JGR Oceans

RESEARCH ARTICLE
10.1029/2023JC020308

Key Points:

- Turbulent Kinetic Energy (TKE) dissipation rates across the interface show a deficit and enhancement supported by the wave field
- A depth integrated subsurface TKE budget highlights the relevance of the transport terms and their connection to wave breaking
- The atmospheric TKE dissipation rate deficit can be explained in terms of wave-induced perturbations mediating energy input to the waves

Correspondence to:
A. Cifuentes-Lorenzen,
alejandro.cifuentes@uconn.edu

Citation:
Cifuentes-Lorenzen, A., Zappa, C. J., Edson, J. B., O'Donnell, J., & Ullman, D. S. (2024). Exploring the role of wave-driven turbulence at the air-sea interface through measurements of TKE dissipation rates across the air-sea interface. *Journal of Geophysical Research: Oceans*, *129*, e2023JC020308. https://doi.org/10.1029/2023JC020308

Received 1 AUG 2023
Accepted 1 AUG 2024

Author Contributions:
Conceptualization: Alejandro Cifuentes-Lorenzen, C. J. Zappa, J. B. Edson, J. O'Donnell
Formal analysis: Alejandro Cifuentes-Lorenzen, C. J. Zappa, J. B. Edson, J. O'Donnell, D. S. Ullman
Funding acquisition: Alejandro Cifuentes-Lorenzen, C. J. Zappa, J. O'Donnell, D. S. Ullman
Investigation: Alejandro Cifuentes-Lorenzen, C. J. Zappa, J. B. Edson, J. O'Donnell
Methodology: Alejandro Cifuentes-Lorenzen, C. J. Zappa, J. B. Edson, J. O'Donnell, D. S. Ullman
Project administration: Alejandro Cifuentes-Lorenzen, C. J. Zappa

© 2024. The Author(s).
This is an open access article under the terms of the Creative Commons Attribution-NonCommercial-NoDerivs License, which permits use and distribution in any medium, provided the original work is properly cited, the use is non-commercial and no modifications or adaptations are made.

Exploring the Role of Wave-Driven Turbulence at the Air-Sea Interface Through Measurements of TKE Dissipation Rates Across the Air-Sea Interface

Alejandro Cifuentes-Lorenzen[1], **C. J. Zappa**[2], **J. B. Edson**[3], **J. O'Donnell**[1], and **D. S. Ullman**[4]

[1]Department of Marine Sciences, University of Connecticut, Storrs, CT, USA, [2]Lamont Doherty Earth Observatory, Columbia University, New York, NY, USA, [3]Applied Ocean Physics and Engineering, Woods Hole Oceanographic Institution, Falmouth, MA, USA, [4]Graduate School of Oceanography, University of Rhode Island, Kingston, RI, USA

Abstract This work serves as an observation-based exploration into the role of wave-driven turbulence at the air-sea interface by measuring Turbulent Kinetic Energy (TKE) dissipation rates above and below the sea surface. Subsurface ocean measurements confirm a TKE dissipation rate enhancement relative to the predicted law-of-the-wall ($\varepsilon_{obs} > \varepsilon_p$), which appears to be fully supported by wave breaking highlighting the role of the transport terms in balancing the subsurface TKE budget. Simultaneous measurements of TKE dissipation rates on the atmospheric side capture a deficit relative to the law-of-the-wall ($\varepsilon_{obs} < \varepsilon_p$). This deficit is explained in terms of wave-induced perturbations, with observed convergence to the law-of-the-wall at 14 m above mean sea level. The deficit on the atmospheric side provides an estimate of the energy flux divergence in the wave boundary layer. An exponential function is used to integrate in the vertical and provide novel estimates of the amount of energy going into the wave field. These estimates correlate well with classic spectral input parameterizations and can be used to derive an effective wave-scale, capturing wind-wave coupling purely from atmospheric observations intimately tied to wave-induced perturbations of the air-flow. These atmospheric and oceanic observations corroborate the commonly assumed input-dissipation balance for waves at wind speeds in the 8-14 ms^{-1} range in the presence of developed to young seas. At wind speeds above 14 ms^{-1} under young seas ($U_{10}/c_p > 1.2$)observations suggest a deviation from the TKE input-dissipation balance in the wave field.

Plain Language Summary A long-term field campaign on the Western North Atlantic shelf provided observations of Turbulent Kinetic Energy (TKE) dissipation rates on both sides of the sea surface. These observations were used to track the energy exchange between the atmosphere and ocean that is mediated by surface waves. Deviations from the expected law-of-the-wall scaling in our TKE dissipation rate estimates were linked to wind energy input leading to wave growth, wave breaking and the subsequent TKE injection into the water column. Observations confirm the subsurface enhancement of TKE relative to the classic law-of-the-wall and showcase a TKE deficit on the atmospheric side. Atmospheric and oceanic TKE dissipation rates converge to the expected law-of-the-wall profiles away from the surface but clearly show the importance of waves in atmosphere-ocean interaction closer to the sea surface. Deviations from the law-of-the-wall are presented as signature of wave-induced turbulence close to the ocean surface.

1. Introduction

The small-scale turbulence at the air-sea interface mediates the transfer of energy, momentum and gases, all of which influence key biogeochemical cycles on Earth. Despite their substantial physical relevance to climate studies, contemporary ocean models cannot numerically resolve the small-scale boundary layer structure due to computational expenses and require specific parameterizations, currently presenting a key challenge to the community. Wave-induced turbulence driven by surface gravity waves has been shown to be a large contributor to upper-ocean mixing, modifying the exchange of momentum, heat, and gases at the air-sea interface (e.g., Melville, 1996) and the deepening of the ocean-mixed-layer (e.g.,Belcher et al., 2012; Li & Fox-Kemper, 2017). Experimental and numerical studies have focused on elucidating the effects and subsurface structure of turbulence driven by wave breaking (e.g., Anis & Moum, 1995; Callaghan, 2018; Gemmrich et al., 1994; Gemmrich & Farmer, 2004; Terray et al., 1996; Thomson et al., 2016) and Langmuir circulation (e.g., Gargett & Wells, 2007; McWilliams et al., 1997; Sullivan et al., 2007; Wu et al., 2019).

Supervision: Alejandro Cifuentes-Lorenzen, C. J. Zappa, J. O'Donnell
Writing – original draft: D. S. Ullman
Writing – review & editing: D. S. Ullman

At present, there is substantial evidence linking wave breaking with a TKE dissipation rate enhancement in the ocean surface layer relative to the law-of-the-wall scaling (e.g., Agrawal et al., 1992; Gemmrich, 2010; Gemmrich & Farmer, 2004; Schwendeman et al., 2013; Terray et al., 1996). Nonetheless, there has been wide variation in the observed vertical structure of the enhancement (e.g., Esters et al., 2018). In the wave-affected layer, Gargett (1989) found a z^{-4} dependence in strongly forced conditions. Craig and Banner (1994) predicted a TKE dissipation rate decay described by $z^{-3.4}$ and, from lake observations, Terray et al. (1996) observed a z^{-2} dependence at depths greater than the significant wave height (H_s) with a constant TKE dissipation rate enhancement above this depth. Sutherland and Kendall Melville (2015) found a z^{-1} dependence close to the surface and a more rapid z^{-2} decay deeper in the water column. More recently Esters et al. (2018) describe the vertical decay as $z^{-1.29}$ over the previously defined transition layer with no clear breaking layer and as $z^{-1.15}$ within the mixed layer, with little variability attributed to wave breaking.

Furthermore, the extent of the enhancement, that is, how deep into the water column the deviations from the law-of-the-wall will reach also exhibits a large degree of uncertainty. This depth has been previously scaled in terms of the significant wave height (e.g., Esters et al., 2018; Gerbi et al., 2008; Terray et al., 1996) with the extent of the enhancement reaching depths 3 to 7 times the significant wave height (e.g.,Toba & Kawamura, 1996). Other work has suggested that the TKE enhancement only extends to a depth that is a fraction of the significant wave height (e.g., Soloviev & Lukas, 2003) with high dissipation values in the near surface region (Sutherland & Kendall Melville, 2015). The overall TKE enhancement and its vertical extent and structure has profound consequences to the TKE budget in the upper ocean, thus affecting mixing and air-sea exchange processes.

On the atmospheric side, away from the air-sea interface, the turbulence behavior conforms to the classic Monin-Obukhov similarity (MOS) theory, where fluxes are independent of height (z) and are universal functions of z/L (e.g., Edson & Fairall, 1998) where L is known as the MOS length, a ratio of mechanical shear production to buoyancy production of turbulence. Nonetheless, close to the air-sea interface wave-induced perturbations can modulate the local turbulence structure, inducing deviations from the classic MOS theory. Evidence of the wave-induced velocities and wave-induced fluxes has been observed (e.g., Grare et al., 2013; Hare et al., 1997; Hristov et al., 2003; Wetzel, 1996), but the vertical structure of these fluxes and their interaction with the mean shear remains elusive.

From this perspective, relevant questions to address are how high do wave-induced perturbations reach on the atmospheric-side and what is the structure of the wave-induced air-flow (e.g., Hara & Sullivan, 2015; Hristov & Ruiz-Plancarte, 2014; Makin & Kudryavtsev, 1999; Mastenbroek et al., 1996). From an air-sea interaction and wave dynamics perspective it is the interaction of the wave-induced perturbations with the air flow that drive wave growth through energy transfer between wind and waves. Early theories of wave growth by Jeffreys (1924), Miles (1957) and Phillips (1957) attempt to address the role and structure of wave-induced perturbations in wave generation and energy transfer. Although the Miles (1957) theory was originally developed under restrictive assumptions (i.e., quasi-laminar flow fields) some key concepts (i.e., critical height and the role of the wind shear profile) are still applicable and of much relevance to the ongoing research on wind-wave coupling and energy exchange. For example, observations by Hristov et al. (2003) aboard the Floating Instrument Platform (FLIP) provide support for the Miles (1957) critical layer theory confirming the relevance of the critical height (z_c), defined as the height where the wind speed matches the wave phase speed, $U(z_c)/_c \sim 1$, for wind-wave coupling. Similarly, through spectral analysis of FLIP data, Grare et al. (2013) show air-flow behavior mostly consistent with the Miles (1957) theory with wave-induced velocities exhibiting a pronounced change in amplitude and phase at the critical height. Nonetheless, above the critical height Grare et al., 2013 observed an upward wave-induced momentum flux that is not fully consistent with the critical layer theory. In this framework, the vertical behavior of wave-induced perturbations can be described as exponential functions with a decay rate proportional to kz where k is the wavenumber with wave-induced perturbations vanishing above the critical layer (e.g., Carpenter et al., 2022; Hristov et al., 2003).

Particle image velocimetry (PIV) systems have been used to study the extent and structure of wave-induced perturbations on the air flow above a wavy surface (e.g., Buckley & Veron, 2016; Carpenter et al., 2022; Reul et al., 1999). For example, based on a tank experiment and a PIV system Shaikh & Siddiqui 2011 showed a rapid vertical decay of the wave-enhanced vorticity above the wave field, with the momentum extraction confined to a shallow layer above the wave field. They concluded that wave-induced perturbations become negligible at heights greater than three times the significant wave height. Buckley and Veron (2016), however, constrained the extent

21699291, 2024, 8, Downloaded from https://agupubs.onlinelibrary.wiley.com/doi/10.1029/2023JC020308 by Christopher J Zappa - Columbia University Libraries , Wiley Online Library on [16/08/2024]. See the Terms and Conditions (https://onlinelibrary.wiley.com/terms-and-conditions) on Wiley Online Library for rules of use; OA articles are governed by the applicable Creative Commons License

of the wave-induced momentum flux to a layer closer to the interface dependent on wavenumber. From an energy flux standpoint, determining the structure and behavior of the wave-induced perturbations, $\tilde{p}(z)$ and $\tilde{w}(z)$, is extremely relevant as the term $\tilde{w}\tilde{p}$ represents wave-induced pressure work and accounts for a flux of energy into (out of) the wave-field that is, the energy flux divergence in the TKE budget, $\partial\langle\tilde{w}\tilde{p}\rangle\big/_{\partial z}$. Recent field work by Zippel et al. (2024) captured the wave-coherent pressure work close to the interface that explains the wind-wave energy input and subsequent growth for young waves. These observations confirm the relevance of the wave-induced perturbations through the wave-coherent pressure work in the wind-wave energy exchange.

Prior investigations have also shown that the sign of the energy flux divergence term on the atmospheric side is related to the state of development of the wave field or wave-age. For example, under older seas (i.e., in the presence of fast moving swells) profiles of TKE dissipation rate from the Air-Sea Interaction Tower (ASIT) during the CBLAST-LOW program (Edson et al., 2007) show how the MOS-predicted values underestimate the observed dissipation rates. Non-locally generated swell aligned with slower overlying winds can drive a reduction and even a reversal of the energy and momentum flux from waves to wind leading to a wave driven wind (e.g., Hanley & Belcher, 2008; Harris, 1966; Semedo et al., 2009; Wu et al., 2019)). Conversely, under growing seas the wind energy transfer into the wave field can lead to a TKE dissipation rate deficit (e.g., Janssen, 1999; Sjöblom & Smedman, 2003) with MOS-predicted values overestimating the dissipation rate. This implies that the inertial dissipation technique (Edson et al., 1991) over the ocean has the potential to underestimate or overestimate the wind stress depending upon the state of the underlying the wave field.

Here, taking advantage of the expected deviations from the rigid-wall scaling on both sides of the air-sea interface, we designed a field experiment to measure TKE dissipation rates in the presence of surface gravity waves under strong forcing conditions. Under actively growing seas, we expected the subsurface TKE dissipation to be enhanced due to wave breaking. On the atmospheric side, the expectation was that under these conditions a TKE dissipation rate deficit, driven mainly by the energy flux divergence $\partial\langle\tilde{w}\tilde{p}\rangle\big/_{\partial z}$ would be evident in measurements close to the interface with wave-induced perturbations strong enough to extend the wave boundary layer (WBL) and offer an opportunity for field measurements to provide a novel insight to the air-sea energy exchange dynamics.

This paper is structured as follows. Section 2 describes the experimental setup and overall conditions during the experiment. Section 3 describes the methods and provides background on the TKE budgets on both sides of the interface. In Section 4 we present our main results. Section 5 presents the discussion and Section 6 our main conclusions.

2. Experimental Setup and Overall Conditions

The ASIT TKE field campaign was designed to be a 3-month atmospheric and oceanographic experiment (Oct 2019–Jan 2020) collecting high temporal resolution measurements close to the air-sea interface. The deployment was intended to capture rough conditions during the Fall-Winter season. The observations on the atmospheric side consisted of micrometeorological profiles of turbulent velocities, momentum fluxes, heat fluxes, pressure, wave breaking statistics and dynamics as well as sea surface displacement and wave spectra. These measurements were collected using Gill Instruments sonic anemometers with a sampling rate of 20 Hz, Paroscientific micro-barometers (10 Hz), RIEGL Laser altimeters (10 Hz), LI-COR open path gas analyzers (10 Hz). The core meteorological data such as air temperature (T_a), relative humidity (RH), and atmospheric pressure were obtained using Campbell Scientific Met-Stations.

TKE dissipation rate profiles above the sea surface were directly estimated from a sonic anemometer array spanning heights of 4.5–22 m above mean sea level (Figure 2). The wind velocity observations from the sonic anemometers were Reynolds averaged and decomposed into turbulent components (i.e., u', v', w'). Turbulent velocities were used to estimate TKE dissipation rates based on the spectral method. Given the fixed nature of the ASIT platform, only wind directions in the 135–270° range were acceptable for processing and analysis to avoid flow distortion introduced by the structure.

The observations on the ocean side of the interface were obtained from instruments on several closely spaced, moored platforms located approximately 1.5 km from the ASIT at the 19 m isobath (Figure 1 and Table 1). An array of 5 Nortek Aquadopp profilers (2 MHz heads) sampling at 4 Hz, measuring fine-scale velocities over a 1 m

21699291, 2024, 8, Downloaded from https://agupubs.onlinelibrary.wiley.com/doi/10.1029/2023JC020308 by Christopher J Zappa - Columbia University Libraries , Wiley Online Library on [16/08/2024]. See the Terms and Conditions (https://onlinelibrary.wiley.com/terms-and-conditions) on Wiley Online Library for rules of use; OA articles are governed by the applicable Creative Commons License

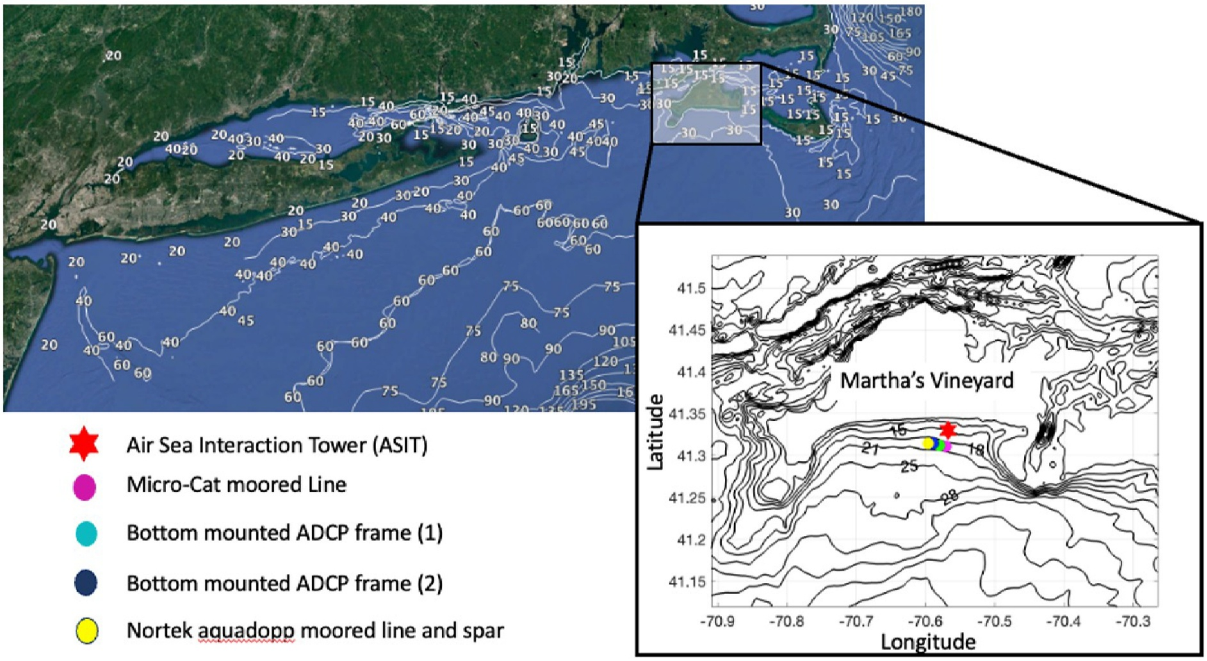

Figure 1. Overview of the deployment configuration for the Air-Sea Interaction Tower (ASIT) Turbulent Kinetic Energy field campaign. White lines in the main image denote the local bathymetry. Black lines in the inset denote the bathymetry of the deployment area. The ASIT tower sits approximately on the 15 m isobath (red star). The subsurface deployment sits approximately along the 19 m isobath (colored circles). The deployment duration spanned Oct 2019–Jan 2020.

range were used to obtain TKE dissipation rate estimates (Figure 1. Nortek Aquadopp moored line and spar). Four of the Aquadopps were attached to a taut-wire mooring at depths of 5, 7, 10 and 15 m below the mean sea surface and the fifth instrument was mounted on a small spar buoy that was tethered to the surface float of the mooring string (Figure 2, right). All Aquadopps were configured to use only one beam to allow for a long-term deployment. Potential interference with the line was accounted for by using instruments with 90° heads (i.e., looking away from the moored line). The spar was designed to host an upward looking Aquadopp and allow for the slanted beam (25°) to be free of frame interference. The spar provided TKE dissipation rate measurements in a wave-following frame of reference. An upward-facing 5-beam Nortek Signature 1,000 kHz ADCP in a gimbaled bottom mount (bottom mounted frame 1, Figure 1), sampling at 8 Hz in 8 min bursts every 30 min, was used to estimate turbulent Reynolds stress profiles in addition to mean velocity profiles, including vertical velocities. A second upward-facing, bottom-mounted 5-beam ADCP (RDI Sentinel 1,200 kHz) was used to obtain directional wave spectra and currents (bottom mounted frame 2, Figure 1). This frame also included a downward looking Nortek Aquadopp profiler (2 MHz) sampling at 4 Hz with a 1 m range that resolved the bottom boundary layer. Water column temperature and salinity measurements were obtained from recording CTDs (SeaBird Microcat) on a mooring with a surface buoy at nominal depths of 0.5, 5, 10, 15 m below the sea surface.

The schematic in Figure 1 shows the deployment configuration along the 19-m isobath and the relative location to ASIT. Figure 2 shows the main arrays used in the deployment to directly measure TKE dissipation rates across the air-sea interface.

Table 1
Subsurface Frames and Moored Lines Location and Depth Recorded From the R/V Connecticut During Deployment

	Latitude	Longitude	Depth m
Nortek aquadopp mooring and spar	41 18.7914	70 34.313	18.5
Bottom mounted frame 2: ADCP RDI sentinel 1,200 kHz, Nortek aquadopp 2 MHz	41 18.7585	70 34.1511	18.5
Bottom mounted frame 1: ADCP Nortek signature 1,000 kHz	41 18.7077	70 33.9275	19.0
Micro-Cat moored line: 4 SeaBird MicroCat CTDs	41 18.6762	70 33.7856	19.0

21699291, 2024, 8, Downloaded from https://agupubs.onlinelibrary.wiley.com/doi/10.1029/2023JC020308 by Christopher J Zappa - Columbia University Libraries , Wiley Online Library on [16/08/2024]. See the Terms and Conditions (https://onlinelibrary.wiley.com/terms-and-conditions) on Wiley Online Library for rules of use; OA articles are governed by the applicable Creative Commons License

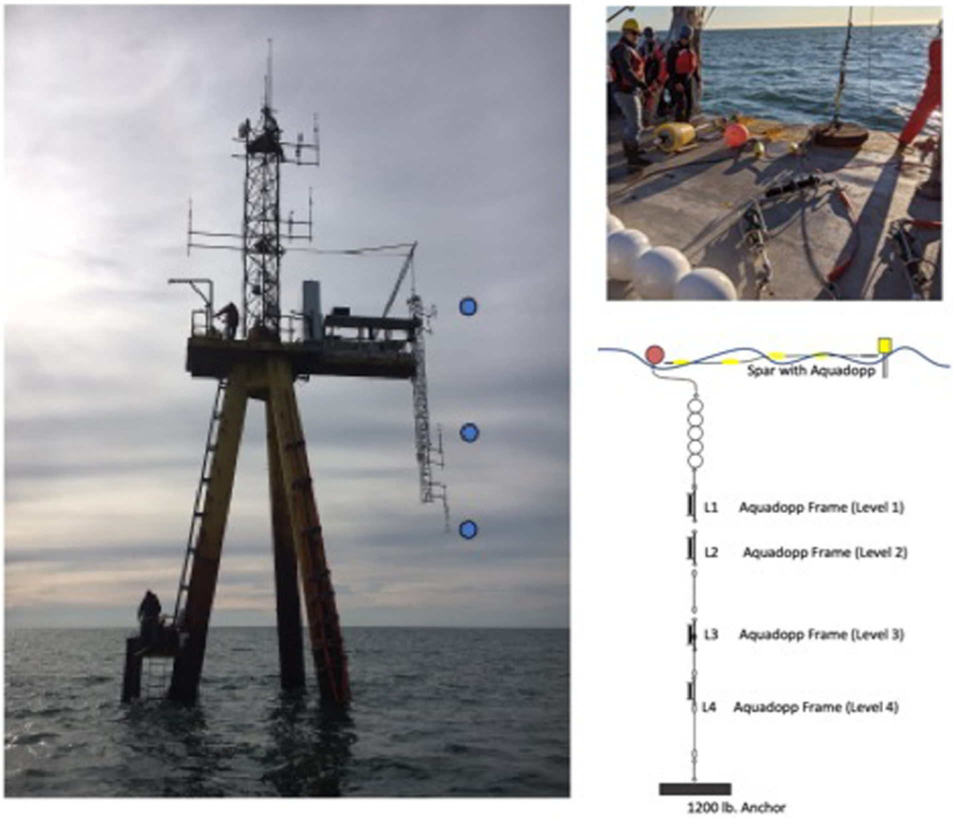

Figure 2. Left hand side, Air-Sea Interaction Tower (ASIT) showing part of the atmospheric array. The sonic anemometers used to capture wave-induced perturbations are marked by the blue circles on the ASIT mast. The sonic anemometers on the mast were 4.5, 8.0 and 14.0 m above mean-sea-level. Right hand side: Spar buoy and moored line of ADCPs deployed. The spar buoy was designed to operate as a wave follower with an array of Aquadopps attached to a taut-wire mooring at depths 5, 7, 10 and 15 below the mean sea. The spar buoy was tethered to the surface float of the mooring string allowing for some drift during the deployment (Figure 2, right).

Figure 2 shows the main arrays used in the deployment to directly measure TKE dissipation rates across the air-sea interface.

The site and the time period of the field campaign allowed sampling over a wide range of wind and wave conditions with periodic strong forcing events. The prolonged and frequent presence of high winds and young, developing seas for both coastal (transitional) and deep-water wave conditions made it an ideal site to address wind-wave generation and air-sea energy exchange in the presence of actively growing waves and consistent wave breaking. The water column experienced overall cooling during the experiment and exhibited weak stratification to fully mixed conditions in late fall/winter, thus limiting buoyancy effects to convective cooling. Currents at the site were driven by barotropic forcing with a dominant M_2 tidal constituent. Surface currents were on average across shelf with the bottom currents oriented along the isobaths with a stronger Eastward (along-shelf) component relative to the Northward component. The vertically averaged Eastward and Northward components ranged between -0.54 and 0.38 ms^{-1} and -0.22 and 0.29 ms^{-1} respectively. Wind speed (U_{10}) was on average 7.33 ms^{-1} with consistent periods of winds above 10 ms^{-1} (Figure 3a) and several events with wind speeds larger than 12 ms^{-1}.

Based on the inverse wave age (U_{10}/c_p) where c_p is the wave phase speed at the spectral peak, the wave field exhibited a wide range of conditions from fully developed to young. For the inverse wave age, values larger (smaller) than 0.82 were considered developing seas (decaying seas) (e.g., Pierson & Moskowitz, 1964). Peak spectral frequency was on average 0.13 Hz (i.e., ~8 s peak wave period) with shorter wind-waves developing

21699291, 2024, 8, Downloaded from https://agupubs.onlinelibrary.wiley.com/doi/10.1029/2023JC020308 by Christopher J Zappa - Columbia University Libraries , Wiley Online Library on [16/08/2024]. See the Terms and Conditions (https://onlinelibrary.wiley.com/terms-and-conditions) on Wiley Online Library for rules of use; OA articles are governed by the applicable Creative Commons License

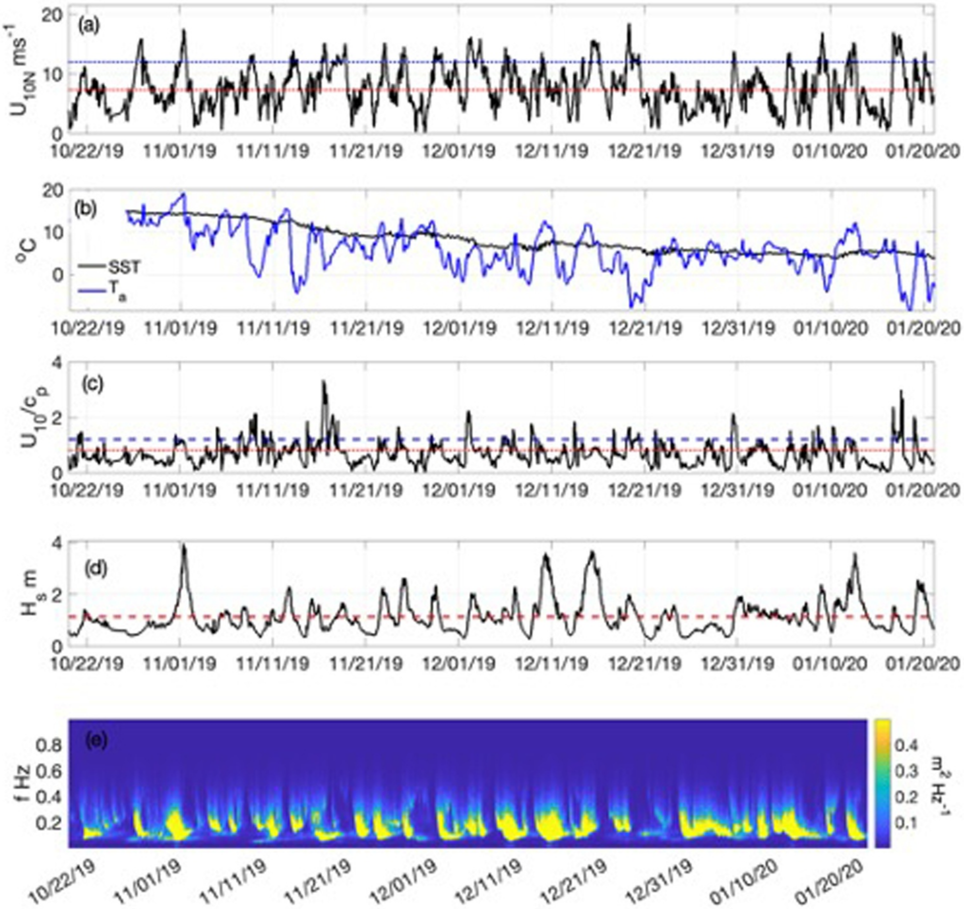

Figure 3. Overall conditions during the Turbulent Kinetic Energy Air-Sea Interaction Tower (ASIT) field campaign 2019–2020. (a) Wind speed recorded at ASIT (10 m neutral). (b) Sea Surface Temperature and air Temperature (10 m reference height) recorded at ASIT (c) inverse wave age (U_{10}/c_p) where c_p is the wave phase speed at the spectral peak derived from frequency spectra from the ADCP 2 at the 19-m isobath. Values larger (smaller) than 0.82 were considered developing seas (decaying seas) red dashed line. Blue dashed line denotes the 1.2 threshold for purely young seas (i.e., actively growing) (d) Significant wave height (H_s) derived from frequency spectra from the ADCP 2 at the 19-m isobath. Red dashed line denotes the average over the experiment of 1.13 ± 0.70 m. (e) Time-frequency wave spectra at the 19-m isobath from bottom mounted ADCP 2.

above 0.2 Hz (i.e., 5 s wave period). Mean significant wave height during the experiment was 1.13 m and reached maximum values above 4.0 m during strong forcing conditions (Figures 3d and 3e).

The wave field development and wave-turbulence regime were characterized using the inverse wave age (U_{10}/c_p) and the Langmuir number (La). For developing seas ($U_{10}/c_p > 0.82$) the energy flux is from wind to waves, supporting wave growth and breaking. Figure 4a shows the probability of occurrence for developing (young) seas conditions. Approximately 40% of the observations were considered to fit our young seas requirement.

The surface Stokes drift, derived from measured wave spectra, was used to define the Langmuir number (Leibovich, 1983) as the ratio of diffusion of streamwise vorticity versus production of streamwise vorticity through Stokes drift. The Langmuir number (squared) can also be stated as (e.g., Belcher et al., 2012), $La = \left(u_*^w/u_s\right)^{1/2}$, where u_*^w is the water-side friction velocity and u_s is the Stokes drift. This ratio was used to identify different turbulence regimes (e.g., Belcher et al., 2012; Noh et al., 2016). The regime during the experiment was on average wind-driven ($La > 0.32$) limiting the role of streamwise vorticity driven by Stokes drift making the Eulerian shear

21699291, 2024, 8, Downloaded from https://agupubs.onlinelibrary.wiley.com/doi/10.1029/2023JC020308 by Christopher J Zappa - Columbia University Libraries , Wiley Online Library on [16/08/2024]. See the Terms and Conditions (https://onlinelibrary.wiley.com/terms-and-conditions) on Wiley Online Library for rules of use; OA articles are governed by the applicable Creative Commons License

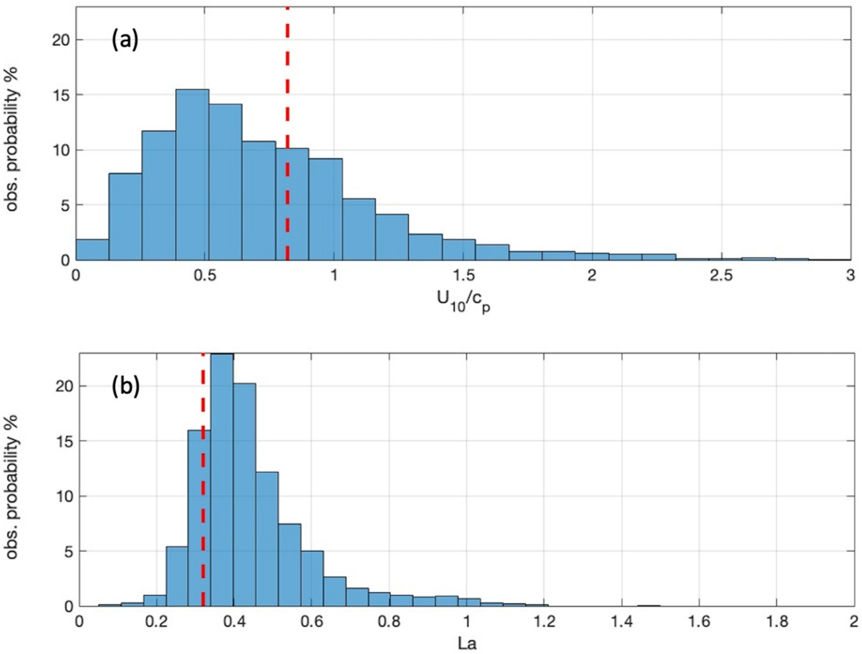

Figure 4. Observed probability of occurrence for inverse wave age (U_{10}/c_p) and Langmuir number (La.) (a) The red dashed line marks the threshold for developed seas $U_{10}/c_p = 0.82$. Values larger than 0.82 are considered developing seas (young). Values lower than 0.82 are considered decaying seas (old). (b) The red dashed line marks the $La = 0.32$ threshold. Values larger than 0.32 are indicative of a wind driven regime, whereas values lower than 0.32 indicate a regime of wave-driven turbulence.

production more relevant (Figure 4b). Less than 30% of the observations fall into the wave-driven turbulence regime.

3. Methods

The experiment targeted observations of TKE dissipation rates in order to investigate the effect of surface gravity waves in the energy transport process by capturing deviations from the rigid-wall scaling. The starting point on both sides of the interface was the TKE budget.

3.1. Atmospheric TKE Budget

Within the surface layer, the momentum and heat fluxes are approximately independent of height and many turbulence-related quantities (e.g., wind shear and temperature gradients) are found to be universal functions of z/L (e.g., Edson & Fairall, 1998). The TKE budget rotated into the main wind direction (i.e., streamwise) under steady-state, horizontally homogeneous and neutral conditions (i.e., negligible buoyancy flux) above a rigid boundary is given by (e.g., Tennekes & Lumley, 1972),

$$-\frac{\partial U}{\partial z}[\langle u'w'\rangle] - \frac{\partial}{\partial z}\left[\frac{1}{\rho_a}\langle w'p'\rangle + \langle e'w'\rangle\right] = \varepsilon \qquad (1)$$

where the angle brackets denote temporal averages and the primes are turbulent fluctuations. On the left-hand side (l.h.s), the first term corresponds to the turbulent shear production, where U and u' are the mean and turbulent components of the streamwise wind velocity and w' is the turbulent component of the vertical velocity with zero mean. The transport terms represent the flux divergence of the pressure work ($\langle w'p'\rangle$) and the vertical flux of TKE ($\langle e'w'\rangle$). The term e' corresponds to the TKE per unit mass (i.e., $e' = \frac{1}{2}\left(u'^2 + w'^2\right)$). Together these terms balance the TKE dissipation rate (ε, m^2 s^{-3}), on the right-hand side (r.h.s). According to previous research, the turbulent transport terms generally cancel one another (e.g., Mcbean & Elliott, 1975; Wyngaard & Coté, 1971),

21699291, 2024, 8, Downloaded from https://agupubs.onlinelibrary.wiley.com/doi/10.1029/2023JC020308 by Christopher J Zappa - Columbia University Libraries , Wiley Online Library on [16/08/2024]. See the Terms and Conditions (https://onlinelibrary.wiley.com/terms-and-conditions) on Wiley Online Library for rules of use; OA articles are governed by the applicable Creative Commons License

leading to a balance between shear production and dissipation. This balance in terms of the law-of-the-wall scaling for TKE dissipation under neutral conditions is given by,

$$\varepsilon = -\frac{\partial U}{\partial z}[\langle u'w'\rangle] = \frac{u_*^3}{\kappa z} \tag{2}$$

where k is the von Karman constant and u_* is the turbulent velocity scaling parameter (i.e., friction velocity).

In the WBL, wave-induced perturbations are expected to be present in the air-flow (e.g., Hare et al., 1997). In the presence of waves, the following decomposition can be applied to the velocity and pressure fields in an effort to include wave-induced perturbations close to the interface,

$$u_i = \langle u\rangle_i + \widetilde{u_i} + u_i' \qquad w = \langle w\rangle + \tilde{w} + w' \qquad \text{and} \qquad p = \langle p\rangle + \tilde{p} + p'$$

where wave-induced perturbations on the airflow are signified by tildes and are supposed to be synchronized with the wave field, that is, coherent. Here, u_i represents the horizontal velocity components ($i = 1{,}2$) and w represents the vertical component. The streamwise decomposition for u can be stated as, $u = U + \tilde{u} + u'$, where U is the mean wind speed in streamwise direction, where $\langle u\rangle = U$ (Equation 3). From a momentum perspective in the WBL the total momentum flux can be stated as,

$$\tau_a = \tau_t + \tau_w + \tau_v$$

where τ_a is the total momentum flux in the layer, τ_t represents the turbulent component, τ_v is the viscous (i.e., tangential stress) and τ_w is the wave induced stress. Note that although τ_a is constant in the WBL it is the partition between τ_t and τ_w that defines the structure of the WBL from a momentum standpoint.

Using the proposed decomposition of turbulent and wave-induced perturbations, the streamwise TKE balance for steady state, homogeneous flow and neutral conditions in the presence of surface gravity waves can then be stated as,

$$-\frac{\partial \mathrm{U}}{\partial \mathrm{z}}[\langle \mathrm{u}'\mathrm{w}'\rangle + \langle \widetilde{\mathrm{u}}\widetilde{\mathrm{w}}\rangle] - \frac{\partial}{\partial \mathrm{z}}\left[\frac{1}{\rho_\mathrm{a}}\langle \mathrm{w}'\mathrm{p}'\rangle + \langle \mathrm{w}'\mathrm{e}'\rangle\right] - \frac{\partial}{\partial \mathrm{z}}\left[\frac{1}{\rho_\mathrm{a}}\langle \widetilde{\mathrm{w}}\widetilde{\mathrm{p}}\rangle + \langle \widetilde{\mathrm{w}}\widetilde{\mathrm{e}}\rangle\right] = \varepsilon \tag{3}$$

On the l.h.s, the first term is the shear production by turbulent and wave induced stresses, the second is the turbulent transport divergence term and the third, arising from wave-induced pressure perturbations, corresponds to the wave-induced energy flux divergence active in the WBL. The term $\tilde{e}$ corresponds to the kinetic energy per unit mass associated with wave-induced perturbations on the air-side (i.e., $\tilde{e} = {}^1\!/\!_2\left(\tilde{u}^2 + \tilde{w}^2\right)$).

Under active energy transfer from wind to waves, there is a non-zero energy flux (3rd term on the l.h.s of Equation 3) into the wave field leading to observations of TKE dissipation rate (ε_{obs}) being smaller than the predicted rigid-wall value (ε_p). From this perspective, there is simply less energy to dissipate. Over growing waves, some of the energy entering the top of the WBL is transferred into the wave field via this flux such that less volume-average dissipation is required to balance the influx. Notice, that this is also consistent with the physical role of this term in wave growth dynamics. The result is a dissipation deficit compared to the law-of-the-wall (e.g., Edson et al., 2007; Janssen, 1999). At the interface the turbulence will eventually dissipate and wave-induced perturbations in coherence with the wave field will support energy and momentum exchange. We hypothesize that the expected TKE dissipation rate deficit is driven by the pressure flux divergence and the wave-induced stress acting over the shear production term representing the work of wave-induced perturbations over the mean flow (i.e., an energy extraction mechanism),

$$\rho_a \Delta\varepsilon = \rho_a[\varepsilon_p - \varepsilon_{obs}] \cong -\left[\frac{\partial}{\partial z}\langle \tilde{w}\tilde{p}\rangle + \rho_a\langle \tilde{u}\tilde{w}\rangle\frac{\partial U}{\partial z}\right] \tag{4}$$

where $\Delta\varepsilon$ corresponds to the difference between the observed and law-of-the-wall predicted dissipation rate. This assumes that the shear and buoyancy production terms are not significantly impacted by the wave field (at least

21699291, 2024, 8, Downloaded from https://agupubs.onlinelibrary.wiley.com/doi/10.1029/2023JC020308 by Christopher J Zappa - Columbia University Libraries , Wiley Online Library on [16/08/2024]. See the Terms and Conditions (https://onlinelibrary.wiley.com/terms-and-conditions) on Wiley Online Library for rules of use; OA articles are governed by the applicable Creative Commons License

above the wave crests) so that their modulation provides a negligible contribution to the dissipation deficit. Equation 4 also neglects the divergence of the transport term $\langle \tilde{w}\tilde{e}\rangle$ relative to $\langle \tilde{w}\tilde{p}\rangle$ as the wave-induced KE (i.e., $\tilde{e}$) is considered small (e.g., Janssen, 1999).

The predicted TKE dissipation rate, $\varepsilon_p = \frac{u_*^3}{\kappa z}\phi_\varepsilon(z/L)$ and the stability function $\phi_\varepsilon(z/L)$ defines the rigid-wall estimate and prediction (e.g., Edson & Fairall, 1998; Kaimal & Finnigan, 1994). Direct estimates of the TKE dissipation rate (ε_{obs}) can be used to estimate the deficit (l.h.s Equation 4), assumed to be a direct consequence of the presence of wave-induced perturbations on the air-flow that is, wave-induced pressure transport (first term r.h.s Equation 4) and energy extraction from the mean flow by wave-induced stress (e.g., Kinsman, 1965) (second term r.h.s Equation 4). Then, integration of Equation 4 over the boundary layer leads to an estimate of the wind-energy input into the wave field,

$$\rho_a \int_{z_l}^{z_h} \Delta\varepsilon \, dz \cong -\int_{z_l}^{z_h} \frac{\partial}{\partial z}\langle \tilde{w}\tilde{p}\rangle \, dz - \int_{z_l}^{z_h} \rho_a \langle \tilde{u}\tilde{w}\rangle \frac{\partial U}{\partial z} dz \tag{5}$$

then,

$$\rho_a \int_{z_l}^{z_h} \Delta\varepsilon \, dz = G_o \tag{6}$$

where z_h is a reference height at which $\Delta\varepsilon$ goes to zero as the wave-induced perturbations vanish and ε_{obs} converges to the predicted value (i.e., rigid-wall scaling). This defines the upper limit of the wave-affected layer from an energy standpoint. The lower integration limit z_l is defined in Section 4.2 relative to MSL. Then from Equation 6 G_o is the wind energy input into the wave field which is equivalent to the spectral form (e.g., Donelan et al., 2006; Gemmrich et al., 1994; Terray et al., 1996):

$$E_{in} = \rho_w \, g \int_\omega \omega\beta(\omega)\, S(\omega)\, d\omega \tag{7}$$

where $S(\omega)$ is the one-dimensional wave spectrum, $\beta(\omega)$ is a wave-growth parameter, ω is the angular frequency ($\omega = 2\pi f$), g is the acceleration due to gravity and ρ_w is the water density.

3.2. Oceanic TKE Budget

The steady-state TKE budget in the water column, under horizontally homogeneous conditions using the Boussinesq approximation can be stated as (e.g., McWilliams et al., 1997):

$$-\langle u_i' w'\rangle \frac{\partial u_i}{\partial z} - \langle u_i' w'\rangle \frac{\partial \langle u_s\rangle}{\partial z} - \frac{g}{\rho_w}\langle \rho' w'\rangle - \frac{\partial}{\partial z}\left[\langle e' w'\rangle + \frac{1}{\rho_w}\langle w' p'\rangle\right] = \varepsilon \tag{8}$$

where primes denote turbulent perturbations and brackets denote temporal averages. Here, u_i are the mean horizontal velocity components ($i = 1, 2$), where the vertical coordinate z is positive upwards and zero at the mean sea surface, u_s is the Stokes drift velocity, u_i' are the horizontal turbulent perturbations and w' is the vertical velocity perturbation. Finally, p' is the turbulent pressure fluctuation, e' is TKE per unit mass (i.e., $e' = \frac{1}{2}\left(u_1'^2 + u_2'^2 + w'^2\right)$) and ρ_w is a constant reference water density. The r.h.s term ε corresponds to the TKE dissipation rate and the four l.h.s terms describe the Eulerian mean shear production, the Stokes shear production, the buoyancy flux, and the divergence of total vertical transport of TKE in the water column, respectively. Here, $\langle e'w'\rangle$ is the TKE flux and $\langle w'p'\rangle$ is the pressure work. The balance in the water column was investigated from an integrated perspective, that is, vertically integrating Equation 8 from the seabed ($-H$) to the surface. The resulting vertically integrated terms in the TKE budget are described in the next sections.

3.2.1. Eulerian Shear Production

The integrated shear production term follows from:

21699291, 2024, 8, Downloaded from https://agupubs.onlinelibrary.wiley.com/doi/10.1029/2023JC020308 by Christopher J Zappa - Columbia University Libraries , Wiley Online Library on [16/08/2024]. See the Terms and Conditions (https://onlinelibrary.wiley.com/terms-and-conditions) on Wiley Online Library for rules of use; OA articles are governed by the applicable Creative Commons License

$$P = \rho_w \int_{-H}^{0} -\langle u_i' w' \rangle \frac{\partial u_i}{\partial z} dz \tag{9}$$

Turbulent Reynolds stresses in the water column were estimated from the bottom frame 1 measurements (5 beam 1,000 kHz Nortek Signature) using the Cospectra-fit method (Gerbi et al., 2008; Kirincich et al., 2010) generalized to the 5-beam case (see Appendix A). The bottom boundary was addressed by incorporating independent estimates of the shear and stress calculated from the bottom frame 2 (downward looking 2 MHz Nortek Aquadopp) resolving the first meter above the seabed. Equation 9 can be rearranged to include the bottom boundary,

$$P = \rho_w \int_{-H}^{0} -\langle u_i' w' \rangle \frac{\partial u_i}{\partial z} dz = \rho_w \left[\int_{-H}^{-z_1} -\langle u_i' w' \rangle_{bott} \frac{\partial u_i}{\partial z}_{bott} dz + \int_{-z_1}^{0} -\langle u_i' w' \rangle \frac{\partial u_i}{\partial z} dz \right] \tag{10}$$

where z_1 is a reference height above the seabed, here $z_1 = -H + 1$ m. The subscript *bott* references the shear and stress in this region (i.e., near-bottom). Bottom stress estimates followed from a log-layer fit and subsequent bottom friction velocity estimate where $\langle u_i' w' \rangle_{bott} \cong \left(u_*^b\right)^2$ based on the assumption of a constant stress layer for $-H : (-H + 1)$. The second term in the r.h.s of Equation 10 integrates the shear production from z_1 to the surface ($z = 0$). Within the final 2–3 m (near-surface), which is not resolved by the ADCP, the velocity was linearly extrapolated to the surface from the last resolved bins of the ADCP. Our extrapolated velocities were consistent with previous observations that have reported surface velocities to be 2%–6% of the wind forcing based on drifters (e.g., Lodise et al., 2019) and 2%–4% based on ADCP, HF radar and drifter buoys for low wind speeds (Sentchev et al., 2017). In this upper layer, the Reynolds stress was assumed to be constant and equal to the estimated wind stress. This approach was justified based on the observed high correlation between estimated Reynolds stresses at the uppermost good ADCP bin and the wind stress (correlation coefficient of 0.84) with a nearly 1:1 relationship between wind stress and the Reynold stresses (see Appendix A3). The presence of a constant stress layer near the surface is also consistent with measurements reported by Scully et al. (2016) based on observations in the Chesapeake Bay in 14 m of water.

3.2.2. Stokes Drift Shear Production

The integrated Stokes drift shear production term follows from,

$$P_S = \rho_w \int_{-H}^{0} -\langle u_i{}' w' \rangle \frac{\partial \langle u_s \rangle}{\partial z} dz \tag{11}$$

where, the frequency-directional wave spectra $S(f, \theta)$ was used to estimate the deep water Stokes drift profile (e.g., Breivik & Christensen, 2020),

$$\boldsymbol{u_s}(z) = \frac{16\pi^3}{g} \int_0^{2\pi} \int_0^{\infty} f^3 \, \hat{\boldsymbol{\theta}} \, e^{2kz} S(f, \theta) \, df d\theta \tag{12}$$

where f and θ are frequency and direction respectively, k is the wavenumber and $\hat{\boldsymbol{\theta}}$ is the unit vector in the direction of wave propagation. The frequency and directional spectra, $S(f, \theta)$ were resolved by the upward looking ADCP in bottom frame (2) with a frequency range between 0.0078 and 1 Hz and frequency resolution of 0.0156 Hz. The spectral tail was extended to 2 Hz using a f^{-5} tail. Direction was equally spaced by 1° intervals with a total of 360 directional bins. As with the estimate of the Eulerian shear production, the Stokes shear production was evaluated assuming a constant Reynolds stress in the upper 2–3 m of the water column based on an air-sea momentum balance as described in Section 3.2.1.

3.2.3. Buoyancy Flux

The surface buoyancy flux (B_0) was estimated using the method presented in Sutherland et al. (2013) and Zhang and Talley (1998). The density flux (Q_p) from the atmosphere into the ocean follows from,

21699291, 2024, 8, Downloaded from https://agupubs.onlinelibrary.wiley.com/doi/10.1029/2023JC020308 by Christopher J Zappa - Columbia University Libraries , Wiley Online Library on [16/08/2024]. See the Terms and Conditions (https://onlinelibrary.wiley.com/terms-and-conditions) on Wiley Online Library for rules of use; OA articles are governed by the applicable Creative Commons License

$$Q_p = \rho(\alpha F_T + \beta F_s) \tag{13}$$

where α and β are the thermal expansion and saline contraction coefficients respectively, ρ is the surface density, F_S and F_T. are given by: $F_T = -Q_{net}/\rho_s C_p$ and $F_S = (E-P)\,S/\left(1-\frac{S}{1000}\right)$. Here, C_p is the water specific heat, and the terms *E, P* and *S* correspond to evaporation, precipitation and surface salinity respectively. The net heat flux (Q_{net}) was obtained from observations at the ASIT tower. Finally, the surface buoyancy flux is given by:

$$B_0 = -gQ_p. \tag{14}$$

We follow Li and Fox-Kemper (2017) and Zippel et al. (2022) in assuming a linear profile of the buoyancy flux, $g\langle\rho'w'\rangle$, throughout the mixed layer. With zero buoyancy flux at the bottom, this gives:

$$-g\langle\rho' w'\rangle \cong B_0 * \left(1 + \frac{z}{H}\right) \tag{15}$$

where H is the total depth of the water column. The depth integrated buoyancy flux is then, $B_0H/2$.

The Monin-Obukhov length scale in the water column can be calculated as (e.g., Sutherland et al., 2013):

$$L = -\frac{(u_*^w)^3}{\kappa B_0} \tag{16}$$

where κ is the von Karman constant. The Monin-Obukhov length in the water column represents the ratio of wind forcing to buoyancy forcing. For a mixed layer depth (D) the ratio $|-L|/D$ can be used to evaluate the relevance of wind driven mixing relative to convective overturning.

During the experiment the water column experienced a cooling trend ($\langle Q_{Net}\rangle > 0$, and a destabilizing buoyancy flux (B). The ratio $|-L|/D$ was on average larger than one (i.e. $|-L|/D > 1$) for a D of 19 m (i.e., entire water column) suggesting that wind forcing was on average dominant over convective overturning in terms of TKE production.

3.2.4. Transport Terms

The transport terms $\langle e'w'\rangle$ and $\langle w'p'\rangle$ correspond to energy and pressure fluxes of TKE,

$$\Gamma(\mathrm{z}) = -\left[\rho_w\langle e'w'\rangle + \langle w'p'\rangle\right] \tag{17}$$

These terms do not produce nor consume TKE, but act to redistribute it. The divergence of these terms was stated as $\partial(\Gamma(\mathrm{z}))/_{\partial z}$, and vertically integrated,

$$\int_{-H}^{0} \partial(\Gamma(\mathrm{z}))/_{\partial z} dz = \Gamma(0) - \Gamma(-\mathrm{H}) \tag{18}$$

At the surface, the transport term $\langle e'w'\rangle_o$ was assumed to be zero (e.g., Scully et al., 2016; Zippel et al., 2022) with the pressure transport term that is, $\langle w'p'\rangle$ being responsible for the downward transport of TKE at the interface (e.g., Scully et al., 2016). For the vertically integrated budget $\Gamma(0)$ can be associated with wind-wave driven input and subsequent wave breaking, where $\Gamma(0) \cong E_{in}$. This implies an input-dissipation balance in the wave field (Section 4). Directly at the interface the wind-input term can be estimated from the estimated wave spectrum (Equation 7),

$$\Gamma(0) \cong E_{in} = \rho_w\, g \int_{\omega} \omega\beta(\omega)\, S(\omega)\, d\omega \tag{19}$$

Finally, at the bottom $\Gamma(-\mathrm{H}) = 0$, assuming no flux through the rigid boundary.

21699291, 2024, 8, Downloaded from https://agupubs.onlinelibrary.wiley.com/doi/10.1029/2023JC020308 by Christopher J Zappa - Columbia University Libraries , Wiley Online Library on [16/08/2024]. See the Terms and Conditions (https://onlinelibrary.wiley.com/terms-and-conditions) on Wiley Online Library for rules of use; OA articles are governed by the applicable Creative Commons License

21699291, 2024, 8, Downloaded from https://agupubs.onlinelibrary.wiley.com/doi/10.1029/2023JC020308 by Christopher J Zappa - Columbia University Libraries , Wiley Online Library on [16/08/2024]. See the Terms and Conditions (https://onlinelibrary.wiley.com/terms-and-conditions) on Wiley Online Library for rules of use; OA articles are governed by the applicable Creative Commons License

Table 2

Averaged, Vertically Integrated Turbulent Kinetic Energy Budget Terms for the Various Ranges of Inverse Wave Age

	$0.82 \le U_{10}/c_p < 1.2$	$1.2 \le U_{10}/c_p < 1.4$	$U_{10}/c_p \ge 1.4$
$\langle U_{10} \rangle$ m s^{-1}	10.3 ± 2.5	10.7 ± 2.6	11.4 ± 2.6
Total production $\langle P_T \rangle$ W m^2	0.0403 (0.004)	0.0313 (0.001)	0.0398 (0.002)
Transport, $\langle \Gamma(0) \rangle$ W m^{-2}	0.524 (0.73)	0.576 (0.92)	0.680 (1.3)
$\langle \varepsilon_D \rangle$ W m^{-2}	0.540 (0.08)	0.640 (0.12)	0.731 (0.15)
$\langle \varepsilon_D - P_T \rangle / \langle \Gamma(0) \rangle$	0.94	1.02	1.05
$\lvert z_T \rvert / \langle H_s \rangle$	−0.21	−0.27	−0.33

Note. The integrated transport term $\langle \Gamma(0) \rangle$ was evaluated using Equation 19 based on the Plant (1982) wave growth parameterization. The data follow log-normal distributions, thus we present the log-mean and the variance in parenthesis. The dimensionless ratio $\lvert z_T \rvert / \langle H_s \rangle$ identifies the shallowest depth at which the TKE dissipation rate could be estimated from the Nortek Aquadopp ADCP on the spar under these conditions.

3.2.5. Turbulent Kinetic Energy Dissipation Rates

TKE dissipation rates were estimated directly from the moored array providing a near surface profile approximately in the [−0.3 −1] m subsurface range and discrete estimates of TKE dissipation rates at approximately −5, −6, −8 and −14 m below the surface.

The TKE dissipation rates within the bottom boundary layer were resolved using the same method relying on a downward looking Nortek Aquadopp and provided estimates within the first meter above the seabed. The depth integrated TKE dissipation rate throughout the water column then follows,

$$Diss = \rho_w \left[\int_{-H}^{-z_1} \varepsilon_{bott}(z)\, dz + \int_{-z_1}^{-z_T} \varepsilon(z)\, dz + \delta_s \varepsilon(z_T) \right] \tag{20}$$

The upper limit $-z_1$ for the bottom TKE dissipation rate estimate (ε_{bott}) was set at approximately 0.75 m above seabed. The upper limit $-z_T$ varied over the deployment and corresponds to the last bin the spar buoy was able to resolve. This depth ($-z_T$) was on average −0.32 m below the sea surface (see $\lvert z_T \rvert / \langle H_s \rangle$ in Table 2). Above it, the TKE dissipation rate was assumed constant for $\delta_s = \lvert z_T \rvert$.

Then, the depth integrated TKE budget, between the bottom and the surface of the water column can be stated as,

$$(P + P_s + B) + \Gamma(0) = Diss \tag{21a}$$

Terms in Equation 21a are plotted for the duration of the experiment (Figure 5) where the integrated TKE dissipation was 1–2 orders of magnitude larger than the production terms,

Figures 5a and 5b show the magnitude of all depth-integrated fluxes in the budget and points out the importance of the transport term at the surface relative to the depth integrated TKE dissipation rate. Mean Eulerian shear production and Stokes shear production are one order of magnitude smaller than the integrated TKE dissipation rate. Figure 5c shows an estimate of the TKE dissipation rate representative of the upper one meter of the water column and contrasts it to the transport term evaluated directly at the surface with both terms being of the same order of magnitude and well correlated.

4. Results

4.1. Subsurface TKE Balance

Throughout the experiment there is a clear TKE dissipation rate enhancement relative to the law-of-the-wall, where production and buoyancy terms cannot by themselves account for it. The transport term at the surface, Γ(0) evaluated as the wind-energy input assumes a wind-input wave-breaking balance, or a so-called input-dissipation balance (e.g., Gemmrich, 2010) The transport follows from a TKE injection mediated by wave breaking and can

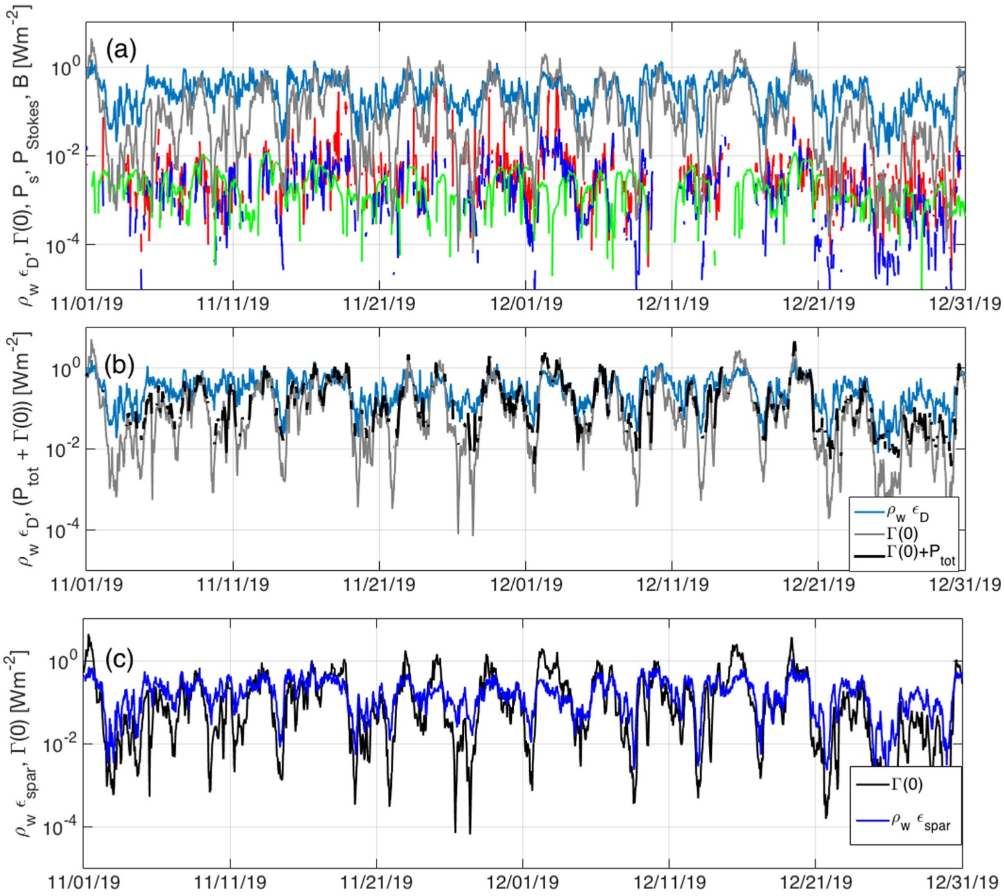

Figure 5. (a) Turbulent Kinetic Energy (TKE) Budget terms Equations 21a and 21b for the entire duration of the experiment. The light blue line shows the depth integrated TKE dissipation rate (*Diss*). The dark blue line corresponds to the Stokes Shear production term (P_S). The red line is the Eulerian shear production (P) term, the green line is the Buoyancy flux (B) and the gray line corresponds to the transport term at the surface Γ(0) estimated using the observed wave spectrum using the Plant, 1982 wave growth parameterization (Equation 19). (b) The light blue line shows the depth integrated TKE dissipation rate (*Diss*), the black line represents the sum of all production terms and the transport term at the surface, and the gray line shows only the transport term at the surface Γ(0). (c) The blue line shows the spar-only depth integrated TKE dissipation rate, representing the total TKE dissipation rate within the first meter of the water column. The black line shows the transport term at the surface Γ(0).

be thought of as a two-step process: (a) energy transfer from wind to waves leading to wave growth and (b) subsequent wave breaking and TKE transfer into the water column.

The required TKE injection to balance the subsurface budget can be alternatively estimated as the difference between the production terms and integrated TKE dissipation rate, that is, $Diss - [(P + P_s) + B]$ (Equation 21b). From this perspective an input-dissipation balance should lead to,

$$Diss - [(P + P_s) + B] = \Gamma(0) \cong E_{in} \tag{21b}$$

where E_{in} follows from Equation 7 and implies that all the energy available to wave growth is injected into the water column through wave breaking resulting in downward transport of TKE. The energy input to the wave field has also been stated in terms of an effective phase speed ($\bar{c}$), capturing the wave-coherent motions at the interface responsible for the energy and momentum exchange (e.g., Cifuentes-Lorenzen et al., 2018; Gemmrich, 2010; Terray et al., 1996). Neglecting the viscous (tangential) stress, the energy input can be written as, $E_{in} = \rho_a u_*^2 \bar{c}$. Although dissipative processes go beyond purely large-scale breaking (e.g., micro-breaking), the assumption presented here is that wind energy input is approximately balanced by overall dissipative processes with large scale breaking being the dominant term under the conditions presented here. Figure 6a shows the depth integrated

21699291, 2024, 8, Downloaded from https://agupubs.onlinelibrary.wiley.com/doi/10.1029/2023JC020308 by Christopher J Zappa - Columbia University Libraries , Wiley Online Library on [16/08/2024]. See the Terms and Conditions (https://onlinelibrary.wiley.com/terms-and-conditions) on Wiley Online Library for rules of use; OA articles are governed by the applicable Creative Commons License

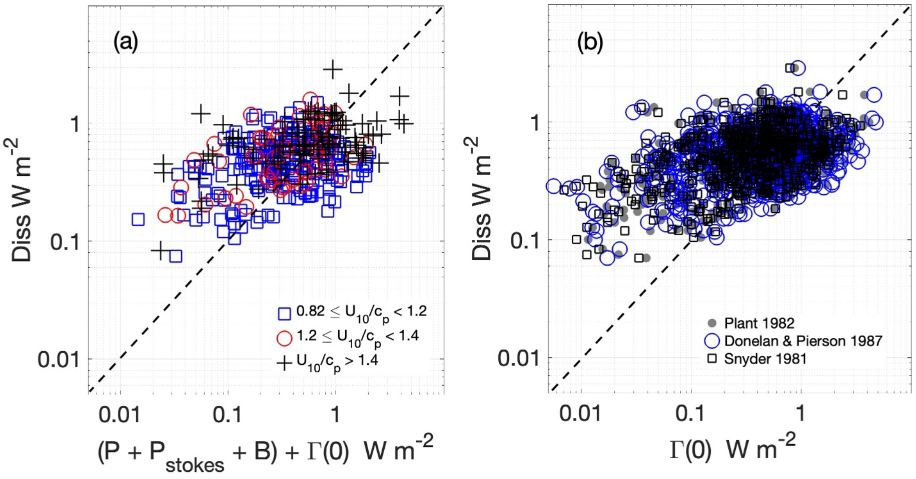

Figure 6. (a) Integrated Turbulent Kinetic Energy (TKE) dissipation rate versus Production and transport terms (Equations 21a and 21b). The black dashed line shows the 1:1 line. Different symbols show the balance for a range of young seas based on the inverse wave age $\left(U_{10}/c_p\right)$ (average wind speed for these conditions was $\langle U_{10N}\rangle = 10.3 \mp 2.5$ m s^{-1}). Blue squares show developed (~0.82) to young seas with an average wind speed $\langle U_{10N}\rangle = 10.7 \mp 2.6$ m s^{-1}. Red circles show young seas in the [1.2–1.4] range. Youngest seas are represented by black plus signs with an average wind speed of $\langle U_{10N}\rangle = 11.4 \mp 2.6$ m s^{-1} (b). Integrated TKE dissipation rate versus Transport term evaluated at the interface using three different wave growth parameterizations (Equation 19).

production terms in the TKE budget plus the transport term in terms of the wind-energy input (Equation 7) against the depth integrated TKE dissipation rate. Figure 6b shows the transport evaluated at the surface using three different wave growth parameterizations (Donelan & Pierson, 1987; Plant, 1982; Snyder et al., 1981) versus the integrated dissipation rate and little difference is seen between them.

These results represent wave field conditions for a range of young seas where the waterside Obukhov Length (L) for the water column ranged between −20.4 and −240.2 m. The ratio $|{-L}|/D$ where D is the depth of the water column (~19.7 m) suggests that wind forcing dominates over buoyancy fluxes throughout the entire water column (i.e., $|{-L}|/D \sim 1$ and $|{-L}|/D >> 1$ respectively). Although the buoyancy flux was not negligible, it was second order in the overall budget. The Langmuir number (La) was on average 0.41 ∓ 0.02 and is thus indicative of weak Langmuir generated vorticity.

Figure 6a suggests an overall subsurface TKE balance when accounting for the wind-driven input mediated by surface gravity waves (i.e., wind-input wave-breaking dissipation balance) with acceptable uncertainty based on the variance of the terms in Equations 21a and 21b (Table 2).

The integrated transport term (Γ(0)) was evaluated at the surface as the wind-energy input to the wave field. Figure 6a and Table 2 emphasize the importance of the air-sea energy exchange in the subsurface TKE budget, with production terms being an order of magnitude lower than the observed TKE dissipation rate for these stages of wave development.

4.2. Wind Energy Input: Wave-Induced Perturbations

Observations show a clear enhancement of the TKE dissipation rate relative to the production terms (Figure 5). The vertically integrated transport term shows the relevance of the wind-driven input in the balance, with the transport closely balancing the input under developing wave conditions (Table 2).

On the atmospheric side, the wind-driven input to the wave field is supported by the pressure flux divergence and the wave-induced stress (Equation 6). These terms are responsible for a TKE dissipation rate deficit relative to the law-of-the-wall (i.e., log-layer $\varepsilon_p(z)$). Figure 7 shows the expected log-layer TKE dissipation rate profile $\varepsilon_p(z)$ and three discrete observations of TKE dissipation rates above MSL (i.e., $\varepsilon_{obs}(z_i)$) based on the data collected by the sonic anemometers (Figure 2). Processing details are described in the Appendix, Section A. Figure (7) suggests that most of the signal (i.e., larger difference between $\varepsilon_p(z)$ and observations) is close to the interface where wave-

21699291, 2024, 8, Downloaded from https://agupubs.onlinelibrary.wiley.com/doi/10.1029/2023JC020308 by Christopher J Zappa - Columbia University Libraries , Wiley Online Library on [16/08/2024]. See the Terms and Conditions (https://onlinelibrary.wiley.com/terms-and-conditions) on Wiley Online Library for rules of use; OA articles are governed by the applicable Creative Commons License

21699291, 2024, 8, Downloaded from https://agupubs.onlinelibrary.wiley.com/doi/10.1029/2023JC020308 by Christopher J Zappa - Columbia University Libraries , Wiley Online Library on [16/08/2024]. See the Terms and Conditions (https://onlinelibrary.wiley.com/terms-and-conditions) on Wiley Online Library for rules of use; OA articles are governed by the applicable Creative Commons License

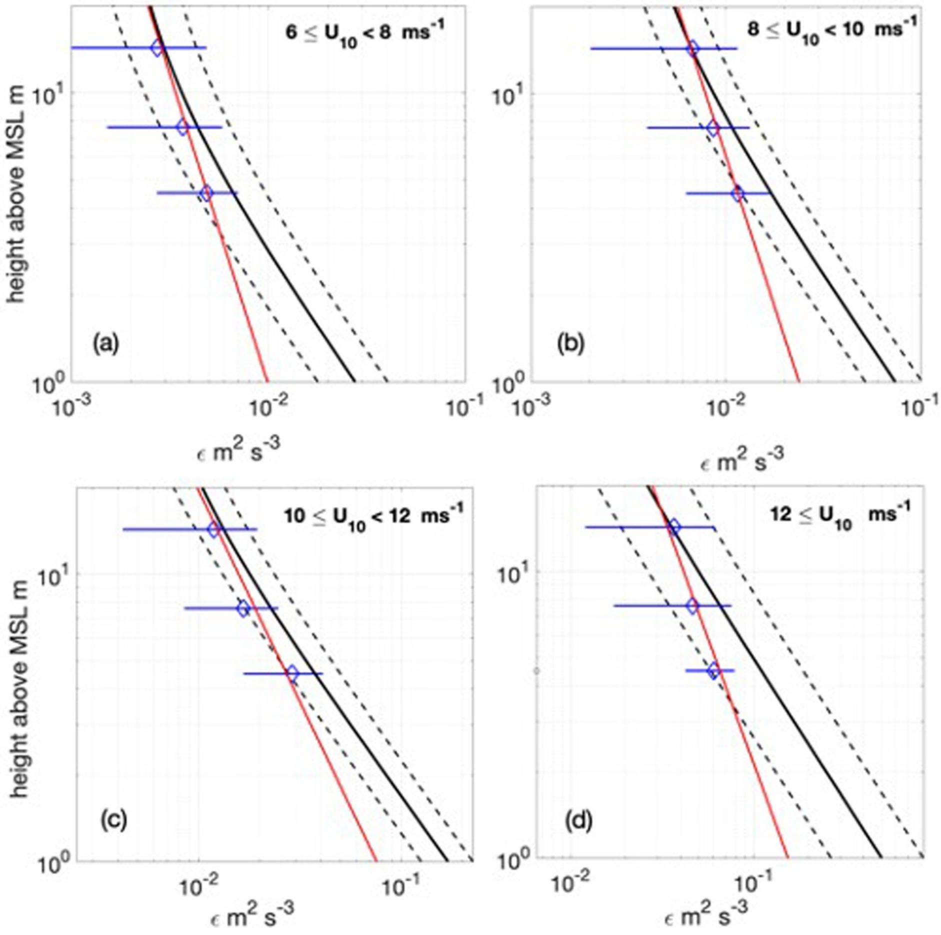

Figure 7. Average atmospheric log-layer Turbulent Kinetic Energy (TKE) dissipation rate profile $\varepsilon_p(z) = \frac{u_*^3}{\kappa z}\phi_\varepsilon(z/L)$ in solid black for different wind ranges. Dashed black lines correspond to ± one standard deviation of $\varepsilon_p(z)$. Predicted values of $\varepsilon_p(z)$ rely on the Edson and Fairall 1998 stability correction function ($\phi_\varepsilon(z/L)$). Blue diamonds are direct estimates of the TKE dissipation rate based on the spectral method and correspond to log-mean values. Blue lines were calculated from the variance in the data from a log-normal distribution and represent the variance of the observations. For $U_{10} < 6$ we observe no difference between predicted and observed TKE dissipation rates (not plotted). On average at 14 m above MSL there is convergence to the law-of-the-wall under all conditions. The red line corresponds to a fit to the observations based on a dimensionless structure, $l_w * \varepsilon_{obs}(z)/F = a\left(z/_{l_w}\right)^n$ Equation 22. See Table 3 for the parameters of the fit.

induced perturbations are expected to be larger. In an effort to capture $\varepsilon_{obs}(z_i)$ closer to the interface and explore the vertical behavior of the wave-induced perturbations through the vertical structure of the TKE dissipation rate we assumed a dimensionless relation in the form,

$$l_w * \varepsilon_{obs}(z)/F = a\left(z/_{l_w}\right)^n \tag{22}$$

where F was directly derived from the average wind energy input, z corresponds to the height above MSL and l_w is a length scale representing the height of the WBL which under these conditions was selected to be 14 m based on observations. Equation 22 borrows the scaling proposed by Terray et al. (1996) and others when studying the subsurface TKE dissipation rate enhancement.

Observations of the TKE dissipation rate showcase the predicted deficit associated with wave-induced perturbations driven by an energy flux into the wave field. Close to the interface (~4.5 and 8 m above MSL), observed TKE dissipation rates were significantly different from the law-of-the-wall values across all wind speed ranges

(Figure 7). Based on a goodness of fit test (chi-squared test) with p-values of 0.90 and 0.20 respectively ($\chi^2 = 4.42$ and 0.44) these differences were considered significant. At 14 m above MSL the same test suggests no difference between observations and the law-of-the-wall predictions that is, p-value of 0.006 ($\chi^2 = 0.012$) consistent with the expected convergence to a rigid-wall scaling at relatively large distances from the wavy sea surface.

Previous work investigating wave-induced perturbations on the air-flow has relied on potential flow theory to model the decay of the perturbations, leading to an exponential function that is, e^{-kz}, where k is the wavenumber and z the height above the interface (e.g., Chalikov & Rainchik, 2011; Jacobs, 1987; Janssen, 1999). Recently, Zippel et al. (2024) based on observations of the wave-coherent pressure and the theoretical work of Janssen (1999) provides an expression in the frequency domain for the wave coherent pressure work that is, $\langle \tilde{w}\tilde{p} \rangle$ with an exponential decay above waves.

Therefore, under the assumption that $\Delta\varepsilon(z_i)$ accounts for the wind energy input purely driven by wave-induced perturbations (Equation 6), we propose an exponential fit to $\Delta\varepsilon(z_i)$ of the form, $\Delta\varepsilon(z) = Aexp(-bz)$, where $\lim\limits_{z\to 14}(\Delta\varepsilon(z)) = 0$ as wave-induced perturbations do not extend above ∼14 m.

Figure 8 shows the fit under different wind regimes with developing to young seas, $U_{10}/c_p \geq 0.82$. Observations and predicted TKE dissipation rate values presented in Figure 7a were statistically different, but had a low χ^2 value (0.22) with a p-value of 0.11 and were not used to define $\Delta\varepsilon(z_i)$. Therefore, we subsampled the wind regime above 12 m s^{-1} (i.e., $12 \leq U_{10}$) and added $12 \leq U_{10} < 14$ m s^{-1} and $U_{10} \geq 14$ m s^{-1} attempting to isolate very strong forcing and young seas, that is, $U_{10}/c_p \sim 1.3$ (Table 3). The fit derived from the expression of the TKE dissipation rate in Equation 22 was used to calculate the TKE dissipation rate at 1 m above MSL and derive the deficit at this height that is, $\Delta\varepsilon(1)$ presented in Figure 8 in the red hexagrams.

Table 4 and Table 5 present the coefficients for the proposed fits, the wind speed range and the mean inverse wave age.

Here, we are constraining the height of the boundary layer to 14 m above MSL (Figure 7) where on average we see no wave-induced perturbations at this height and consider this to represent the upper limit of the WBL from an energy standpoint. This defines the upper integration limit in Equation 6 (i.e., z_h). The lower integration limit (i.e., z_l) was defined as 0.5 m above MSL. This is approximately half of the mean significant wave height (i.e., mean wave amplitude) and was considered representative of the average surface displacement. We then integrate $\Delta\varepsilon(z)$ over the height [0:14] m above MSL where below 0.5 m the deficit was considered constant. Assuming the exponential behavior between [0:14] m with no constant TKE deficit below 0.5 m leads to estimates of energy fluxes that are larger by approximately 6%. Our current observations cannot resolve this layer nor address the TKE dissipation rate structure in this near surface region. Nonetheless, the proposed method provides energy input estimates consistent with wave growth parameterizations without an a priori calibration or imposing any constraints. In this framework the proposed two-layer structure on the atmospheric side resembles the observed subsurface TKE dissipation structure.

Figure 9a shows a comparison of the wind energy input derived using wave spectra (Equation 7) evaluated using three different wave growth parameterizations and the empirical G_o function (Equation 6) that captures wave-induced perturbations and the energy flux based on the TKE dissipation rate deficit,

$$G_o = \rho_a \int_{z_l}^{z_h} \Delta\varepsilon \, dz + \rho_a z_l \Delta\varepsilon(z_l) \tag{23}$$

The proposed coefficients for the exponential fit, $\Delta\varepsilon(z) = Aexp(-bz)$ are presented in Table 4 with the results plotted in Figure 9. Figure 9a shows G_o (Equation 23) as a function of wind speed and three wind-energy input terms as a function of wind speed relying on different wave growth parameterizations.

Estimates of G_o based on an exponential decay (Table 4) show good agreement with spectral estimates of the wind input (Figure 9a). The middle range estimates are consistent with all three wave growth parameterizations ($10 \leq U_{10} < 14$ ms^{-1}). These estimates are also consistent with the difference between integrated TKE dissipation rate and production terms (i.e., $\langle Diss - P_T \rangle$) (Figure 9b) and corroborate a wind energy input—wave breaking dissipation balance in this range of wave development.

21699291, 2024, 8, Downloaded from https://agupubs.onlinelibrary.wiley.com/doi/10.1029/2023JC020308 by Christopher J Zappa - Columbia University Libraries , Wiley Online Library on [16/08/2024]. See the Terms and Conditions (https://onlinelibrary.wiley.com/terms-and-conditions) on Wiley Online Library for rules of use; OA articles are governed by the applicable Creative Commons License

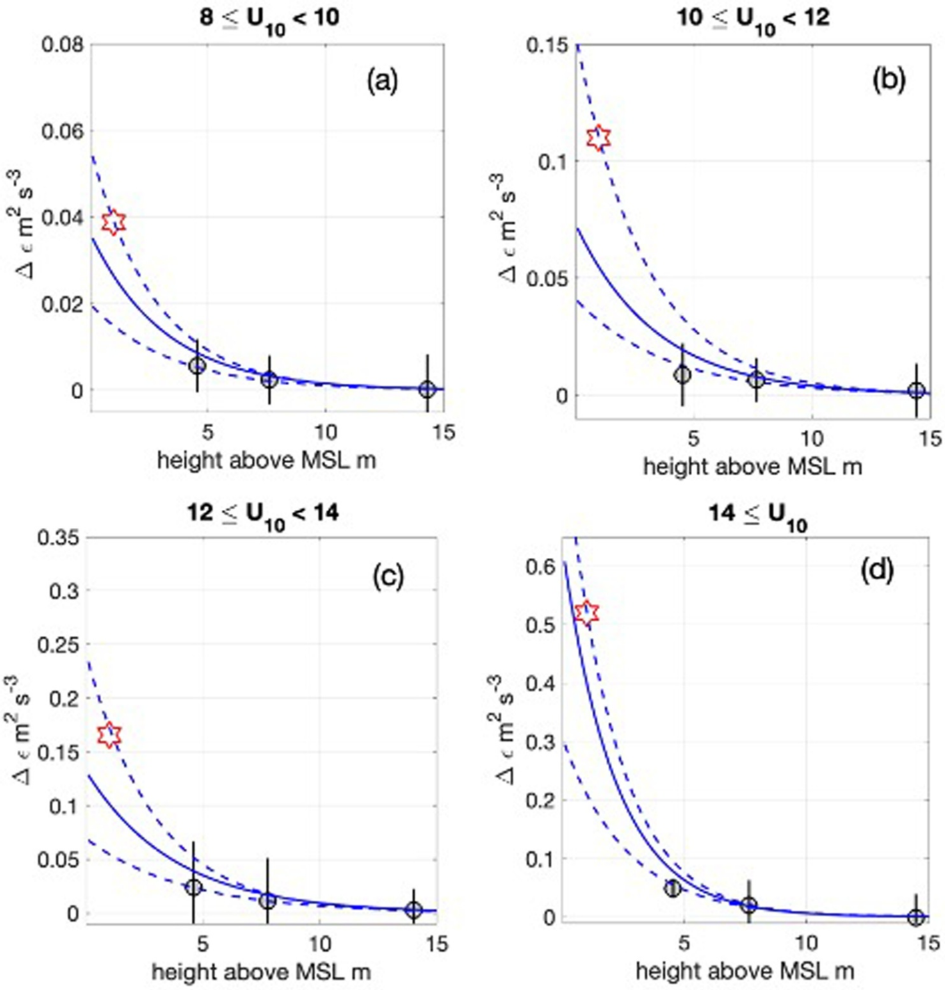

Figure 8. The functional behavior of $\Delta\varepsilon(z)$ based on the fit: $\Delta\varepsilon(z) = Aexp(-bz)$, where $\lim_{z\to 14}(\Delta\varepsilon(z)) = 0$. Black and gray circles correspond to the Turbulent Kinetic Energy (TKE) dissipation rate deficit based on direct estimates from sonic spectra derived at three levels. Red hexagram is the TKE dissipation rate deficit estimated from the fit of the observations, $l_w * \varepsilon_{\text{obs}}(z)/F = a\left(z/_{l_w}\right)^n$ at 1 m above MSL relative to the law-of-the-wall. Blue solid lines represent the best fit to all TKE deficit estimates and is considered to represent the mean behavior of $\Delta\varepsilon(z)$. A fit that minimizes the residual of the lowest estimate (i.e., red hexagram) was used to calculate and constrain the upper bound of the energy input. A fit minimizing the residual of the estimate at ~4.5 m above MSL without the lowest value (i.e., red hexagram) was used to calculate the lower bound of the energy input. The fits to the upper and lower bounds are shown by the dashed blue lines and are presented to illustrate the uncertainty in the estimate of Equation 22.

Table 3
Fitted Parameters for the Function $l_w * \varepsilon_{obs}(z)/F = a\left(z/_{l_w}\right)^n$, *Where* l_w *Was Fixed at 14 m and F Was Evaluated From* E_{in} *as* $F = \langle E_{in}\rangle/\rho_w$

	$6 \leq U_{10} < 8$	$8 \leq U_{10} < 10$	$10 \leq U_{10} < 12$	$12 \leq U_{10}$
a	6.81×10^2	5.83×10^2	5.00×10^2	5.32×10^2
n	−0.458	−0.483	−0.698	−0.529

Note. TKE dissipation rate observations for the fit were derived from the spectral method at all levels. Below *a*,*n* are the coefficients used in in Figure 7.

The lowest estimate of G_o (i.e., $8 \leq U_{10} < 10$ ms^{-1}) for developed to developing seas agrees well with the Donelan and Pierson (1987) wave growth parameterization (within 20% on the mean) but is low relative to the other two parameterizations. Part of the wave-induced signal under these conditions could have been missed by the deployment configuration (i.e., wave-induced perturbations closer to the interface). Nonetheless, Figure 9b shows the difference between integrated TKE dissipation rate and production terms (i.e., $\langle Diss - P_T\rangle$) to be consistent with G_o (within 30%). Finally, under the strongest forcing presented here ($U_{10} \geq 14$) with the youngest seas recorded, the mean G_o estimate driven by wave-induced perturbations is 35% larger than the largest spectral estimate of the wind-energy input and 62% larger than the required

21699291, 2024, 8, Downloaded from https://agupubs.onlinelibrary.wiley.com/doi/10.1029/2023JC020308 by Christopher J Zappa - Columbia University Libraries , Wiley Online Library on [16/08/2024]. See the Terms and Conditions (https://onlinelibrary.wiley.com/terms-and-conditions) on Wiley Online Library for rules of use; OA articles are governed by the applicable Creative Commons License

Table 4
Coefficients for the Fit, $\Delta\varepsilon(z) = A\exp(-bz)$

U_{10} m s^{-1}	$8 \leq U_{10} < 10$	$10 \leq U_{10} < 12$	$12 \leq U_{10} < 14$	$U_{10} \geq 14$
$\left\langle U_{10}/c_p \right\rangle$	0.87	1.03	1.18	1.29
A m^2 s^{-3}	0.0362	0.0828	0.132	0.637
b m^{-1}	0.329	0.310	0.264	0.462

Note. Mean fit, solid blue lines Figures 8a–8d.

TKE to balance the subsurface budget that is, $\langle Diss - P_T \rangle$) (Figure 9b). This observed deviation from the input-dissipation balance at high wind speeds was also observed by Thomson et al. (2016) and could potentially suggest that under these conditions the input-dissipation balance between wind-input and wave breaking does not hold anymore with waves actively growing and retaining some of the energy imparted by the wind.

5. Discussion

This work serves as an observation-based exploration into the role of wave-driven turbulence at the air-sea interface through measurements of TKE dissipation rates. The field campaign was conducted under moderate to strong forcing over the Western North Atlantic shelf and provided TKE dissipation rates above and below the interface. Subsurface TKE dissipation rates were estimated using a Nortek Aquadopp ADCP mounted on a wave-following spar buoy in combination with a moored line of Nortek Aquadopps. Subsurface TKE dissipation rates were estimated to be one to two orders of magnitude above the law-of-the wall estimates, that is, $\varepsilon_{obs} > \varepsilon_p$. Depth integrated observations of the TKE dissipation rate remained high throughout the experiment (Figure 5). The depth integrated TKE budget suggests a balance between the TKE transport terms and the dissipation rate with all other terms being one to two orders of magnitude smaller. This suggests that the shear production (Eulerian velocity and Stokes drift) and buoyancy terms cannot account for the observed enhancement, highlighting the relevance of energy exchange and air-sea interaction mediated by the wave field.

The transport terms in the TKE budget were redefined as, $\Gamma(z) = -[\rho_w \langle ew' \rangle + \langle w'p' \rangle]$ where vertical integration allows for evaluation at the boundaries leading to, $\Gamma(-Z) = 0$ at the bottom and $\Gamma(0) = E_{in}$ at the surface. Here, $\Gamma(0)$ is directly linked to the wind energy input (E_{in}) transferred into the water column mediated by wave breaking. This injection of TKE at the surface is physically related to the subsurface pressure transport term that is, $\langle w'p' \rangle$ as discussed by Scully et al. (2016) and is required to balance the subsurface TKE budget.

The Eulerian shear production close to the surface was estimated by linearly extrapolating the velocity from the uppermost bins of the ADCP measurements and assuming constant shear stress in this layer. The constant stress layer assumption in the upper region of the water column was supported by estimates of the Reynolds stress (∼15.5 m above the bed) in good agreement with wind stress estimates (i.e., τ_a). The comparison is presented in Figure A1 in the Appendix. The slope of the linear regression between these quantities is reported as 0.82 and therefore reasonably close to the value of one expected in the case of constant stress in the layer above the uppermost good bin. The approximate 1:1 relationship across the air-sea interface was also reported by Scully et al. (2016) in Chesapeake Bay in 14 m of water at a depth of ∼1.5 m below the surface.

Estimates of surface velocities based on a linear extrapolation agree with previously reported surface velocities as a fraction of the wind speed. For example, the average wind-driven surface velocity has been reported to be 2%–6% of the wind speed based on drifters under strong wind forcing conditions (e.g., Lodise et al., 2019) and 2%–4% based on an ADCP, HF radar and drifter buoys for low wind speeds (Sentchev et al., 2017). Our extrapolated surface velocities correspond to 2%–4% of the observed wind speed placing the estimate with previous observations. Finally, preliminary results from infra-red imaging at the ASIT site during the experiment support the magnitude of the surface currents derived from the linear extrapolation.

Therefore, in the absence of any field observations of the near surface shear structure under active wave breaking conditions and due to the difficulty of the measurement itself we propose this as a reasonable approximation. The constant stress layer assumption in the near-surface region was also used to estimate the Stokes shear production relying on the Stokes velocity profile retrieved from spectral observations.

Table 5
Coefficients for the Fit, $\Delta\varepsilon(z) = A\exp(-bz)$

U_{10} m s^{-1}	$8 \leq U_{10} < 10$	$10 \leq U_{10} < 12$	$12 \leq U_{10} < 14$	$U_{10} \geq 14$
$\left\langle U_{10}/c_p \right\rangle$	0.87	1.03	1.18	1.29
A m^2 s^{-3}	0.055	0.155	0.242	0.849
b m^{-1}	0.344	0.338	0.335	0.482

Note. Max fit, upper limit blue dashed lines Figures 8a–8d

Finally, we emphasize that the subsurface depth integrated TKE balance is mainly between the TKE dissipation rate and the transport terms evaluated in terms of the wind-input (Table 2) with production terms being 10–20 times smaller (Figure 5).

Simultaneous measurements of TKE dissipation rates on the atmospheric side capture a deficit relative to the law-of-the-wall ($\varepsilon_{obs} < \varepsilon_p$), consistent with

21699291, 2024, 8, Downloaded from https://agupubs.onlinelibrary.wiley.com/doi/10.1029/2023JC020308 by Christopher J Zappa - Columbia University Libraries , Wiley Online Library on [16/08/2024]. See the Terms and Conditions (https://onlinelibrary.wiley.com/terms-and-conditions) on Wiley Online Library for rules of use; OA articles are governed by the applicable Creative Commons License

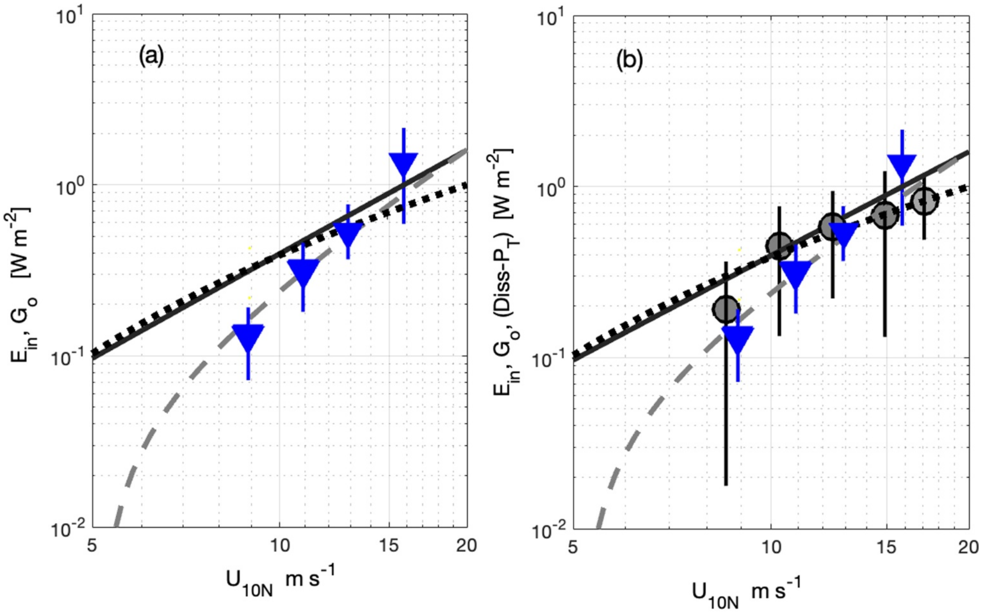

Figure 9. Estimates of wind energy input to the wave field as a function of wind speed. Turbulent Kinetic Energy (TKE) dissipation rate deficit-based estimates, that is, $G_o = \int_{0.5}^{14} \rho_a \Delta\varepsilon(z_i)\, dz$, are shown as triangles. Wave age increases with wind speed $\left\langle U_{10}/c_p \right\rangle$), 0.87, 1.03, 1.18 and 1.29 respectively. The solid black line is based on the Plant (1982) wave growth parameterization, the gray dashed line is based on the Donelan and Pierson (1987) parameterization and the dotted black line denotes the Snyder et al. (1981) parameterization. Figure 9b. The gray circles represent the energy input required to close the subsurface TKE budget, that is, vertically integrated TKE dissipation rate minus production terms, $\langle Diss - P_T \rangle$.

previous observations by Edson et al. (2007) and with theoretical arguments of the wave-induced energy fluxes (Janssen, 1999). Observations of the TKE dissipation rate were significantly lower than law-of-the-wall predictions close to the interface (~4.5 and 8 m above MSL) for the upper wind speed regimes, but not for low wind speeds (less than 6 m s^{-1}). Across wind forcing we observe no wave-induced signal at 14 m above MSL. These observations were used to define the dimensionless structure of the TKE dissipation rate on the atmospheric side. Borrowing from subsurface turbulence studies we proposed, $l_w * \varepsilon_{obs}(z)/F = a\left(z/l_w\right)^n$, where F corresponds to the wind energy input and l_w was defined as a length scale representing the height of the WBL which under these conditions was selected to be 14 m and set as a constant. Table 3 presents the coefficients for the regression. Based on this fit we extrapolated the TKE dissipation rate to the interface to retrieve information and define the TKE dissipation rate deficit at 1 m above MSL (Figure 8). Direct observations and the proposed extrapolation provided four discrete heights with estimates of the TKE dissipation rate deficit. The deficit was explained in terms of wave-induced perturbations in coherence with surface waves and linked to the energy flux into the wave field. Mechanistically these correspond to the pressure flux divergence in terms of the wave-coherent pressure work (e.g., Zippel et al., 2024) and the wave-induced stress acting over the wind shear term (e.g., Kinsman, 1965) (Equation 4). These observations cannot fully discern the relative importance of these terms in the overall input, but we hypothesize that energy flux divergence through pressure work is of leading order. This is consistent with recent results presented by Zippel et al. (2024) showing direct estimates of the wave-coherent pressure work in good agreement with independent estimates of wind energy input. Nonetheless, we speculate that the wave-induced stress related flux (i.e., $\langle \tilde{u}\tilde{w} \rangle \frac{\partial U}{\partial z}$) may be relevant closer to the interface as it is supported by shorter wave scales (e.g., Grare et al., 2013). A full evaluation of the term would also require either prescribing or capturing the structure of the shear profile close to the interface (e.g., Janssen & Bidlot, 2023). Ideally future efforts in the field would attempt to tackle this question.

Regardless, the vertical integration of the TKE dissipation rate deficit provided an estimate of the wind energy input to the wave field, that is, G_o in Equation 23. Integration of the deficit that is, $\Delta\varepsilon(z)$ was based on the proposed exponential function (Tables 4 and 5) and shows good agreement with classic spectral input

21699291, 2024, 8, Downloaded from https://agupubs.onlinelibrary.wiley.com/doi/10.1029/2023JC020308 by Christopher J Zappa - Columbia University Libraries , Wiley Online Library on [16/08/2024]. See the Terms and Conditions (https://onlinelibrary.wiley.com/terms-and-conditions) on Wiley Online Library for rules of use; OA articles are governed by the applicable Creative Commons License

parameterizations (Equation 7). Results are presented in (Figure 9). Estimating G_o using Table 5 provides an upper bound of the energy input to the wave-field derived solely from atmospheric observations. Although, these observations were able to capture wave-induced perturbations above and away from the interface, it is clear that a large fraction of the signal is below 4.5 m (MSL) making this type of measurement in the field extremely difficult.

From a wave action standpoint we find that the integrated input-dissipation balance holds for wind speeds in the 10–14 ms^{-1} range with inverse wave ages (U_{10}/c_p) denoting young seas (1.03–1.18). This is consistent with the subsurface TKE budget estimate of the TKE required to balance the budget (Figure 9b) expressed in terms of the transport at the interface $\Gamma(0)$. This assumes all energy going into wave growth is injected as TKE through wave breaking. Above 14 m s^{-1} winds, the integrated TKE deficit (i.e., G_o) is larger than the required transport needed to close the subsurface TKE budget ($\Gamma(0)$) and larger than the spectral estimate (E_{in}, Equation 7). We speculate that in this regime waves are actively growing, with only a fraction of the spectral input going into dissipation in the water column. Based on these results we hypothesize that under young seas $\left(U_{10}/c_p > 1.2\right)$ the input-dissipation balance may not hold or deviate and should be further evaluated in an effort to address energy partitioning and wave dynamics under strong forcing conditions.

6. Conclusions

By resolving TKE dissipation rates above and below the surface we indirectly addressed the role of surface gravity waves in the energy transfer across the air-sea interface. Observations show deviations from the law-of-the-wall on both sides of the interface with a subsurface enhancement and atmospheric deficit relative to the rigid-wall scaling. Enhanced subsurface TKE dissipation rates were placed in context by accounting for the wind energy input and wave breaking in the vertically integrated TKE budget. Closing the integrated TKE budget in the water column required the transport term evaluated at the surface that is, $\Gamma(0)$ to account for the wind energy input and the subsequent TKE injection into the water column through wave breaking. Production and buoyancy terms were found to be second order to the required transport term at the interface.

Simultaneous measurements of TKE dissipation rates on the atmospheric side captured a deficit relative to the law-of-the-wall predictions ($\varepsilon_{obs} < \varepsilon_p$). The deficit was explained as a direct consequence of wave-induced perturbations modifying the airflow and extending up to approximately 10 m above MSL with observed convergence to the law-of-the-wall at 14 m above MSL. Observations of the TKE dissipation rates (i.e., ε_{obs}) with convergence to the law-of-the-wall at 14 m were used to evaluate a dimensionless function describing the vertical structure of the TKE dissipation rate that is, $l_w * \varepsilon_{obs}(z)/F = a\left(z/l_w\right)^n$ (Table 3). This was then used to provide a dissipation estimate at 1 m above MSL and add one more data point to derive a fit describing the functional behavior of the deficit away from the interface that is, $\Delta\varepsilon(z) = A\exp(-bz)$ and provide estimates of the wind energy input driving the observed TKE dissipation rate deficit. Wave-induced perturbations could not be resolved nor observed for wind speeds below 6 m s^{-1} and suggest a shallower WBL. The proposed estimates of energy input are consistent with spectral parameterizations in the 8–14 ms^{-1} range and demonstrate the importance of wave-induced perturbations at the air-sea interface and the need to incorporate them in air-sea parameterizations and atmosphere-ocean models in an effort to understand the air-sea exchange mechanisms.

Finally, the input-dissipation balance holds for wind speeds in the 8–14 ms^{-1} range for young seas ($0.82 < U_{10}/c_p \leq 1.2$). Above 14 ms^{-1} with inverse ages indicative of younger seas ($U_{10}/c_p > 1.2$) we observe a deviation from the input-dissipation balance based on the TKE deficit method and hypothesize that in this regime waves actively grow and retain a larger fraction of the energy and therefore a smaller fraction of the wind energy input goes into dissipation.

Appendix A: Processing Methodologies

A1. TKE Dissipation Rates From Sonic Anemometers

For estimating TKE dissipation rates from the sonic anemometers that is, ε_{obs} in Equation 4 the wind direction was constrained to the range: $135 \leq W_{dir} \leq 270$. This range ensures no flow distortion on the sonics. Processing was

21699291, 2024, 8, Downloaded from https://agupubs.onlinelibrary.wiley.com/doi/10.1029/2023JC020308 by Christopher J Zappa - Columbia University Libraries , Wiley Online Library on [16/08/2024]. See the Terms and Conditions (https://onlinelibrary.wiley.com/terms-and-conditions) on Wiley Online Library for rules of use; OA articles are governed by the applicable Creative Commons License

performed over 20-min segments with a sampling frequency of 20 Hz (24,000 data points). The spectral method was applied to retrieve ε_{obs} in the inertial subrange (e.g., Fairall & Larsen, 1986).

The relationship between the TKE dissipation rate and the spectral density (in the wavenumber domain) in the inertial subrange follows directly from Kolmogorov:

$$F(k) = \alpha \varepsilon^{2/3} k^{-5/3} \tag{A1}$$

Equation 8 can be stated in the frequency domain after using Taylor's frozen-field hypothesis and correcting for wind speed variability past the sensor (Wyngaard & Clifford, 1977). For example, Charuchittipan & Wilson, 2009) suggest applying the Wyngaard and Clifford (1977) correction to account for the variability of the eddies being advected past the sensor that is, accounting for enhanced turbulence intensity when applying the frozen-field hypothesis. The correction (T_{11}) can be stated as,

$$T_{11} = 1 - \frac{\overline{u'^2}}{9U^2} + \frac{2\overline{v'^2}}{3U^2} + \frac{2\overline{w'^2}}{3U^2} \tag{A2}$$

where U is the mean wind speed and *u', v'* and *w'* correspond to the x, y and z turbulent components of the wind speed. Piper and Lundquist (2004) also suggest using this correction when applying the spectral method to estimate TKE dissipation rates. Relying on the frozen-field hypothesis and the correction presented in Equation A2 we can restate Equation A1 as,

$$f\ S(f) = T_{11}\ \alpha\ \varepsilon^{2/3} \left(\frac{2\pi f}{U}\right)^{-2/3} \tag{A3}$$

Finally, Freire et al. (2019) proposed a transfer function to estimate the effect of path averaging on synthetic data. The transfer function ($H(f, U, p)$) where p corresponds to the path length for the sonic anemometer (i.e., distance between transmit-receive).

Here, U is the wind speed and f is the frequency. Additionally, Henjes (1997) also accounts for aliasing and path averaging and introduced two attenuation functions in terms of wind speed and a path length (p) and derived a

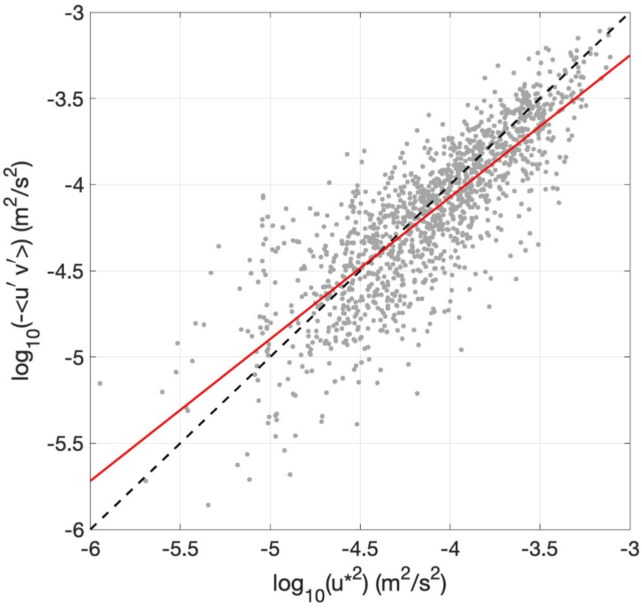

Figure A1. Log-values of Reynolds stress (y-axis) versus log-values of wind stress (x-axis). The 1:1 line is shown in dashed black with the linear regression in solid red. The regression slope is 0.82.

21699291, 2024, 8, Downloaded from https://agupubs.onlinelibrary.wiley.com/doi/10.1029/2023JC020308 by Christopher J Zappa - Columbia University Libraries , Wiley Online Library on [16/08/2024]. See the Terms and Conditions (https://onlinelibrary.wiley.com/terms-and-conditions) on Wiley Online Library for rules of use; OA articles are governed by the applicable Creative Commons License

Transfer function $H(f, U, p)$. Here a single path length (p) of 0.15 m was used. Then the corrected spectral density ($S(f)$) can be sated in terms observed spectral density ($S_{obs}(f)$),

$$S(f) = S_{obs}(f)\, H(f, U, p) \tag{A4}$$

Finally, the observed TKE dissipation rates from the sonic anemometer spectra follows from Equation A4,

$$\varepsilon_{obs} = \frac{2\pi}{U}\left[\frac{f^{\frac{5}{3}} S(f)}{T_{11\ \alpha}}\right]^{3/2} \tag{A5}$$

where ε_{obs} is the observed TKE dissipation rate on the atmospheric side. Each sonic anemometer (Figure 2) was used to provide an estimate of Equation A5 above the interface providing a $\Delta\varepsilon(z)$ at different heights.

A2. Subsurface TKE Dissipation Rates

TKE dissipation rates were derived from Nortek Aquadopp instruments mounted on the moored line (Figure 2). Sampling frequencies were set at 4–8 Hz with bin sizes of 25 mm. The first 1.5 m of the water column was profiled with an upward looking Nortek Aquadopp (Figure 2) mounted on a spar buoy (e.g., Thomson, 2012). The spar buoy was designed to act as a wave follower and deployed to allow some drifting while tethered to the moored line. The processing operates over the beam velocity coordinate of the Nortek Aquadopp, where only one beam was operational to allow for a longer-term deployment than could be achieved if all beams were used. The instrument was deployed with the only objective of resolving the inertial subrange of the turbulence to calculate the TKE dissipation rate using the second order structure function and the spectral method (not presented here). The sampling frequency was set at 4 Hz for the 1 MHz head collecting 512 profiles over a burst time of 2.33 min. The 2 MHz head sampled at 8 Hz collecting 1,024 profiles over a 2.33-min burst. The beam velocity was then unwrapped and a correlation threshold of 60% was empirically defined and imposed before processing. The bin size was set at 25 mm with a 2 m range.

Profiles of the TKE dissipation rates were estimated from the center-differenced turbulence structure function ($D(z, r, t)$) following Wiles et al. (2006) and Gemmrich (2010). The structure function depends on time, depth, and separation between the measurements of turbulent fluctuations of velocity,

$$D(z, r, t) = \left\langle \left(v'\left(z - \frac{r}{2}, t\right) - v'\left(z + \frac{r}{2}, t\right)\right)^2 \right\rangle \tag{A6}$$

With the TKE dissipation rate (ε) calculated as (e.g., Gemmrich, 2010),

$$\varepsilon(z,t) = C^{-3/2}\, r^{-1} D(z, r, t)^{3/2} \tag{A7}$$

where $C = 2.0$ (Frehlich & Cornman, 2002). The separations between differenced velocities, r, are restricted to the inertial sub-range, constrained by the Kolmogorov (l_K) and Ozmidov (l_O) length scales (i.e., $l_K \ll s \ll l_O$). In practice, the separations and admitted scales of motion are dictated by the size of the depth bins in the velocity profiles. Each burst provides a time step (t) with n velocity profiles that can be averaged to provide a TKE dissipation rate profile estimate: $\varepsilon(z, t)$. A least squares fit of a first-degree polynomial is made to $D(z,r)$ for different depths ($z_1, z_2, z_3, \ldots z_m$) where m is the number of bins used in the processing.

$$D(z_i, r) = A\, r^{2/3} + Noise \tag{A8}$$

Where the coefficient $A = C^2 \varepsilon^{2/3}$ and for $Noise \ll Ar^{2/3}$

$$D(z_i, r) = A\, r^{2/3} \tag{A9}$$

Structure function estimates were cross-validated at all depths with the spectral method (Zippel et al., 2022).

21699291, 2024, 8, Downloaded from https://agupubs.onlinelibrary.wiley.com/doi/10.1029/2023JC020308 by Christopher J Zappa - Columbia University Libraries , Wiley Online Library on [16/08/2024]. See the Terms and Conditions (https://onlinelibrary.wiley.com/terms-and-conditions) on Wiley Online Library for rules of use; OA articles are governed by the applicable Creative Commons License

21699291, 2024, 8, Downloaded from https://agupubs.onlinelibrary.wiley.com/doi/10.1029/2023JC020308 by Christopher J Zappa - Columbia University Libraries , Wiley Online Library on [16/08/2024]. See the Terms and Conditions (https://onlinelibrary.wiley.com/terms-and-conditions) on Wiley Online Library for rules of use; OA articles are governed by the applicable Creative Commons License

A3. Subsurface Reynold Stresses

Turbulent Reynolds stresses, in an environment of episodically strong surface gravity waves, were estimated from the bottom-mounted Nortek ADCP measurements using the Cospectra-fit method (Gerbi et al., 2008; Kirincich et al., 2010) generalized to the 5-beam case. The ADCP recorded data at 8 Hz in beam coordinates with instrument pitch and roll recorded at the full ping rate, allowing for the application of bin-mapping (Dewey & Stringer, 2015) on each ping. The ADCP also recorded pressure at 8 Hz, and as described below, this signal was used in determining the frequency band in which surface gravity wave velocities were significant. Following Dewey and Stringer (2015), at each vertical ADCP bin, the set of equations relating cartesian velocity components to the five tilted beam velocities was used to form five equations relating the five measured along-beam variances and the six components of the stress tensor. Assuming that the horizontal stress component, $\overline{u'v'}$ is negligible (Lu & Lueck, 1999), the system of equations can be solved for the remaining five stress components. To apply the Cospectra-fit method, we utilize the Fourier transform of these equations, which provides the vertical stress cospectra and the autospectra of the three cartesian velocity components in terms of the beam velocity autospectra. Autospectra of the bin-mapped beam velocities were computed using the multitaper spectral method (e.g., Park et al., 1987).

The Cospectra-fit method to estimate Reynolds stresses (e.g., $\overline{u'w'}$) was applied to cospectra rotated into downwind (u) and crosswind (v) components and converted to wavenumber spectra with the frozen field assumption for turbulence using the burst-mean velocity magnitude. The fitting of an empirical function for the cospectra (Kaimal et al., 1972; Kirincich et al., 2010),

$$Co_{uw}(k) = \overline{u'w'}\left(\frac{7}{3\pi}\sin\frac{3\pi}{7}\right)\frac{1/k_o}{1+\left({}^{k}/_{k_o}\right)^{7/3}} \tag{A10}$$

was performed using only measured cospectral estimates at frequencies below the gravity wave band, which was determined by comparing the measured vertical beam (vertical velocity) autospectra to vertical velocity autospectra computed from the spectra of pressure assuming linear gravity waves. Following Gerbi et al. (2008), the cutoff frequency, the low frequency boundary of the wave band, was determined as the lowest frequency at which the wave vertical velocity spectrum exceeded 30% of the measured vertical velocity spectrum. Fitting of the nonlinear Kaimal et al. (1972) cospectrum, was performed using MATLAB's *lsqcurvefit* function using the “trust-region-reflective” search algorithm. Experimentation with different initial guesses for the two parameters of the Kaimal cospectrum, the Reynolds stress and the so-called roll off wavenumber (the wavenumber of the dominant energy-containing eddies, k_o in A10), indicated that the optimal solutions found by the search algorithm were not dependent upon the initial values.

For the analysis reported here, Reynolds stress estimates were screened in several ways. Following Gerbi et al. (2008), we removed estimates for which wave contamination of the low-frequency portion of the spectra could be important using the ratio of the wave orbital velocity (estimated from the pressure signal) to the burst-mean drift velocity. Estimates for which the wave velocity was greater than twice the magnitude of the drift velocity were screened out. Second, we screened out estimates for which the roll off wavenumber was outside the range spanned by the minimum resolved wavenumber of the cospectrum and the high wavenumber limit determined by the wave cutoff wavenumber. Third, we removed all stress estimates from bursts during which the standard deviation of pitch or roll exceeded 0.5 deg. Finally, we required that the fit of the empirical cospectrum explained 90% or more of the variance in the observed cospectrum.

Finally, Reynolds stress estimates that satisfied the screening at the ADCP bin 15.5 m above bottom, the uppermost good bin, were compared to the wind stress derived from the atmospheric observations (Figure A1). The slope of the linear regression between these quantities (red line in Figure A1) is 0.82 and therefore reasonably close to the value of one expected in the case of constant stress in the layer above the uppermost good bin. This comparison serves as a validation for the constant stress layer assumption used to estimate the vertically integrated production terms in the TKE budget.

21699291, 2024, 8, Downloaded from https://agupubs.onlinelibrary.wiley.com/doi/10.1029/2023JC020308 by Christopher J Zappa - Columbia University Libraries , Wiley Online Library on [16/08/2024]. See the Terms and Conditions (https://onlinelibrary.wiley.com/terms-and-conditions) on Wiley Online Library for rules of use; OA articles are governed by the applicable Creative Commons License

Data Availability Statement

The manuscript relies on observations from the ASIT TKE field campaign covering a three-month period (Oct 2019–Jan 2020). The experiment combines atmospheric and oceanographic data. The ASIT tower was equipped with sonic anemometers, laser altimeters, high frequency pressure sensors and met stations for atmospheric pressure, air temperature and RH. The tower provides high frequency sonic anemometer data with turbulent fluctuations u', v', w' and T' at 20 Hz. High frequency sonic data was used to estimate TKE dissipation rates above the interface. The tower also provides air-sea fluxes from the COARE bulk algorithm and eddy covariance estimates of heat and momentum fluxes, wind speed and direction among other meteorological and oceanographic variables (Edson et al., 2024). The subsurface measurements consisted of an array of ADCPs and CTDs along the 19-m isobath. A moored line of ADCPs and a surface following spar buoy provides estimates of subsurface TKE dissipation rates. These instruments collected currents, wave statistics, water temperature, and salinity at discrete depths and were used to derive production and dissipation terms in the TKE budget (Cifuentes-Lorenzen et al., 2024). All data processing and quality control relied on the Matlab software (The MathWorks Inc, 2022).

Acknowledgments

This material is based upon work supported by the National Science Foundation under NSF Award 1756789 titled: Collaborative Research: Investigating the Air-Sea Energy Exchange in the presence of Surface Gravity Waves by Measurements of Turbulence Dissipation, Production and Transport.

References

Agrawal, Y. C., Terray, E. A., Donelan, M. A., Hwang, P. A., Williams, A. J., Drennan, W. M., et al. (1992). Enhanced dissipation of kinetic energy beneath surface waves. *Nature*, *359*(6392), 219–220. https://doi.org/10.1038/359219a0

Anis, A., & Moum, J. N. (1995). Surface wave–turbulence interactions. Scaling ε(z) near the sea surface. *Journal of Physical Oceanography*, *25*(9), 2025–2045. https://doi.org/10.1175/1520-0485(1995)025<2025:SWISNT>2.0.CO;2

Belcher, S. E., Grant, A. L. M., Hanley, K. E., Fox-Kemper, B., Van Roekel, L., Sullivan, P. P., et al. (2012). A global perspective on Langmuir turbulence in the ocean surface boundary layer. *Geophysical Research Letters*, *39*(18). https://doi.org/10.1029/2012GL052932

Breivik, Ø., & Christensen, K. H., (2020). A combined stokes drift profile under swell and wind sea. *Journal of Physical Oceanography*, *50*(10), 2819–2833. https://doi.org/10.1175/JPO-D-20-0087.1

Buckley, M. P., & Fabrice, V. (2016). Structure of the airflow above surface waves. *Journal of Physical Oceanography*, *46*(5), 1377–1397. https://doi.org/10.1175/JPO-D-15-0135.1

Callaghan, A. H. (2018). On the relationship between the energy dissipation rate of surface-breaking waves and oceanic whitecap coverage. *Journal of Physical Oceanography*, *48*(11), 2609–2626. https://doi.org/10.1175/JPO-D-17-0124.1

Carpenter, J. R., Buckley, M. P., & Veron, F. (2022). Evidence of the critical layer mechanism in growing wind waves. *Journal of Fluid Mechanics*, *948*(October), A26. https://doi.org/10.1017/jfm.2022.714

Chalikov, D., & Rainchik, S. (2011). Coupled numerical modelling of wind and waves and the theory of the wave boundary layer. *Boundary-Layer Meteorology*, *138*(1), 1–41. https://doi.org/10.1007/s10546-010-9543-7

Charuchittipan, D., & Wilson, J. D. (2009). Turbulent kinetic energy dissipation in the surface layer. *Boundary-Layer Meteorology*, *132*(2), 193–204. https://doi.org/10.1007/s10546-009-9399-x

Cifuentes-Lorenzen, A., Edson, J. B., & Zappa, C. J. (2018). Air–Sea interaction in the southern ocean: Exploring the height of the wave boundary layer at the air–sea interface. *Boundary-Layer Meteorology*, *169*(3), 461–482. https://doi.org/10.1007/s10546-018-0376-0

Cifuentes-Lorenzen, A., Zappa, C. J., Ullman, D., O'Donnell, J., & Edson, J. B. (2024). *ASIT TKE experiment: Observations 2019-2020 ocean*. Zenodo. https://doi.org/10.5281/zenodo.12824154

Craig, P. D., & Banner, M. L. (1994). Modeling wave-enhanced turbulence in the ocean surface layer. *Journal of Physical Oceanography*, *24*(12), 2546–2559. https://doi.org/10.1175/1520-0485

Dewey, R., & Stringer. (2015). Reynolds stresses and turbulent kinetic energy estimates from various ADCP beam configurations. *Theory*. https://doi.org/10.13140/RG.2.1.1042.8002

Donelan, M. A., Babanin, A. V., Young, I. R., & Banner, M. L. (2006). Wave-follower field measurements of the wind-input spectral function. Part II: Parameterization of the wind input. *Journal of Physical Oceanography*, *36*(8), 1672–1689. https://doi.org/10.1175/JPO2933.1

Donelan, M. A., & Pierson, W. J., Jr. (1987). Radar scattering and equilibrium ranges in wind-generated waves with application to scatterometry. *Journal of Geophysical Research*, *88*(C7), 4381–4392. https://doi.org/10.1029/JC092iC05p04971

Edson, J., Cifuentes-Lorenzen, A., Zappa, C. J., O'Donnell, J., & Ullman, D. (2024). *ASIT TKE experiment: Observations 2019-2020 atmosphere*. Zenodo. https://doi.org/10.5281/zenodo.12802958

Edson, J., Crawford, T., Crescenti, J., Farrar, T., Nelson, F., Gerbi, G., et al. (2007). The coupled boundary layers and air–sea transfer experiment in low winds. *Bulletin of the American Meteorological Society*, *88*(3), 341–356. https://doi.org/10.1175/BAMS-88-3-341

Edson, J. B., & Fairall, C. W. (1998). Similarity relationships in the marine atmospheric surface layer for terms in the TKE and scalar variance budgets. *Journal of the Atmospheric Sciences*, *55*(13), 2311–2328. https://doi.org/10.1175/1520-0469(1998)055<2311:SRITMA>2.0.CO;2

Edson, J. B., Fairall, C. W., Mestayer, P. G., & Larsen, S. E. (1991). A study of the inertial-dissipation method for computing air-sea fluxes. *Journal of Geophysical Research*, *96*(C6), 10689–10711. https://doi.org/10.1029/91jc00886

Esters, L., Breivik, Ø., Landwehr, S., ten Doeschate, A., Sutherland, G., Christensen, K. H., et al. (2018). Turbulence scaling comparisons in the ocean surface boundary layer. *Journal of Geophysical Research: Oceans*, *123*(3), 2172–2191. https://doi.org/10.1002/2017JC013525

Fairall, C. W., & Larsen, S. E. (1986). Inertial-dissipation methods and turbulent fluxes at the air-ocean interface. *Boundary-Layer Meteorology*, *34*(3), 287–301. https://doi.org/10.1007/BF00122383

Frehlich, R., & Cornman, L. (2002). Estimating spatial velocity statistics with coherent Doppler Lidar. *Journal of Atmospheric and Oceanic Technology*, *19*(3), 355–366. https://doi.org/10.1175/1520-0426-19.3.355

Freire, L., Dias, N., & Chamecki, M. (2019). Effects of path averaging in a sonic anemometer on the estimation of turbulence-kinetic-energy dissipation rates. *Boundary-Layer Meteorology*, *173*(October), 99–113. https://doi.org/10.1007/s10546-019-00453-4

Gargett, A. E. (1989). Ocean turbulence. *Annual Review of Fluid Mechanics*, *21*(1), 419–451. https://doi.org/10.1146/annurev.fluid.21.1.419

Gargett, A. E., & Judith, R. W. (2007). Langmuir turbulence in shallow water. Part 1. Observations. *Journal of Fluid Mechanics*, *576*, 27–61. https://doi.org/10.1017/S0022112006004575

Gemmrich, J. (2010). Strong turbulence in the wave crest region. *Journal of Physical Oceanography*, *40*(3), 583–595. https://doi.org/10.1175/2009JPO4179.1

Gemmrich, J. R., & Farmer, D. M. (2004). Near-surface turbulence in the presence of breaking waves. *Journal of Physical Oceanography*, *34*(5), 1067–1086. https://doi.org/10.1175/1520-0485(2004)034<1067:NTITPO>2.0.CO;2

Gemmrich, J. R., Mudge, T. D., & Polonichko, V. D. (1994). On the energy input from wind to surface waves. *Journal of Physical Oceanography*, *24*(11), 2413–2417. https://doi.org/10.1175/1520-0485(1994)024<2413:OTEIFW>2.0.CO;2

Gerbi, G. P., Trowbridge, J. H., Edson, J. B., Plueddemann, A. J., Terray, E. A., & Fredericks, J. J. (2008). Measurements of momentum and heat transfer across the air–sea interface. *Journal of Physical Oceanography*, *38*(5), 1054–1072. https://doi.org/10.1175/2007JPO3739.1

Grare, L., Lenain, L., & Kendall Melville, W. (2013). Wave-coherent airflow and critical layers over ocean waves. *Journal of Physical Oceanography*, *43*(10), 2156–2172. https://doi.org/10.1175/JPO-D-13-056.1

Hanley, K. E., & Belcher, S. E. (2008). Wave-driven wind jets in the marine atmospheric boundary layer. *Journal of the Atmospheric Sciences*, *65*(8), 2646–2660. https://doi.org/10.1175/2007JAS2562.1

Hara, T., & Sullivan, P. P. (2015). Wave boundary layer turbulence over surface waves in a strongly forced condition. *Journal of Physical Oceanography*, *45*(3), 868–883. https://doi.org/10.1175/JPO-D-14-0116.1

Hare, J. E., Hara, T., Edson, J. B., & Wilczak, J. M. (1997). A similarity analysis of the structure of airflow over surface waves. *Journal of Physical Oceanography*, *27*(6), 1018–1037. https://doi.org/10.1175/1520-0485(1997)027<1018:ASAOTS>2.0.CO;2

Harris, D. L. (1966). The wave-driven wind. *Journal of the Atmospheric Sciences*, *23*(6), 688–693. https://doi.org/10.1175/1520-0469(1966)023<0688:TWDW>2.0.CO;2

Henjes, K. (1997). Isotropic and anisotropic correlations in turbulent wind speed data. *Boundary-Layer Meteorology*, *84*(July), 149–167. https://doi.org/10.1023/A:1000386716341

Hristov, T., & Ruiz-Plancarte, J. (2014). Dynamic balances in a wavy boundary layer. *Journal of Physical Oceanography*, *44*(12), 3185–3194. https://doi.org/10.1175/JPO-D-13-0209.1

Hristov, T. S., Miller, S. D., & Friehe, C. A. (2003). Dynamical coupling of wind and ocean waves through wave-induced air flow. *Nature*, *422*(6927), 55–58. https://doi.org/10.1038/nature01382

Jacobs, S. J. (1987). An asymptotic theory for the turbulent flow over a progressive water wave. *Journal of Fluid Mechanics*, *174*, 69–80. https://doi.org/10.1017/S0022112087000041

Janssen, P. A. E. M. (1999). On the effect of ocean waves on the kinetic energy balance and consequences for the inertial dissipation technique. *Journal of Physical Oceanography*, *29*(3), 530–534. https://doi.org/10.1175/1520-0485(1999)029<0530:OTEOOW>2.0.CO;2

Janssen, P. A. E. M., & Jean-Raymond, B. (2023). Wind–wave interaction for strong winds. *Journal of Physical Oceanography*, *53*(3), 779–804. https://doi.org/10.1175/JPO-D-21-0293.1

Jeffreys, H. (1924). On the formation of water waves by wind. *Proceedings of the Royal Society of London - Series A: Containing Papers of a Mathematical and Physical Character*, (Vol. 107(742), 189–206).

Jr Pierson, W. J., & Moskowitz, L. (1964). A proposed spectral form for fully developed wind seas based on the similarity theory of S. A. Kitaigorodskii. *Journal of Geophysical Research*, *69*(24), 5181–5190. https://doi.org/10.1029/JZ069i024p05181

Kaimal, J. C., & Finnigan, J. J. (1994). *Atmospheric boundary layer flows: Their structure and measurement*. Oxford University Press. https://doi.org/10.1093/oso/9780195062397.001.0001

Kaimal, J. C., Wyngaard, J. C., Izumi, Y., & Coté, O. R. (1972). Spectral characteristics of surface-layer turbulence. *Quarterly Journal of the Royal Meteorological Society*, *98*(417), 563–589. https://doi.org/10.1002/qj.49709841707

Kinsman, B. (1965). *Wind waves, their generation and propagation on the ocean surface*. Prentice-Hall.

Kirincich, A. R., Lentz, S. J., & Gerbi, G. P. (2010). Calculating Reynolds stresses from ADCP measurements in the presence of surface gravity waves using the cospectra-fit method. *Journal of Atmospheric and Oceanic Technology*, *27*(5), 889–907. https://doi.org/10.1175/2009JTECHO682.1

Leibovich, S. (1983). The form and dynamics of Langmuir circulations. In *Annual review of fluid mechanics*. Annual Reviews. https://doi.org/10.1146/annurev.fl.15.010183.002135

Li, Q., & Fox-Kemper, B. (2017). Assessing the effects of Langmuir turbulence on the entrainment buoyancy flux in the ocean surface boundary layer. *Journal of Physical Oceanography*, *47*(12), 2863–2886. https://doi.org/10.1175/JPO-D-17-0085.1

Lodise, J., Özgökmen, T., Griffa, A., & Berta, M. (2019). Vertical structure of ocean surface currents under high winds from massive arrays of drifters. *Ocean Science*, *15*(6), 1627–1651. https://doi.org/10.5194/os-15-1627

Lu, Y., & Lueck, R. G. (1999). Using a broadband ADCP in a tidal channel. Part I: Mean flow and shear. *Journal of Atmospheric and Oceanic Technology*, *16*(11), 1556–1567. https://doi.org/10.1175/1520-0426(1999)016<1556:UABAIA>2.0.CO;2

Makin, V. K., & Kudryavtsev, V. N. (1999). Coupled sea surface-atmosphere model: 1. Wind over waves coupling. *Journal of Geophysical Research*, *104*(C4), 7613–7623. https://doi.org/10.1029/1999JC900006

Mastenbroek, C., Makin, V., Garat, M. H., & Giovanangeli, J.-P. (1996). Experimental evidence of the rapid distortion of turbulence in the air flow over water waves. *Journal of Fluid Mechanics*, *318*(-1), 273. https://doi.org/10.1017/s0022112096007124

Mcbean, G. A., & Elliott, J. A. (1975). The vertical transports of kinetic energy by turbulence and pressure in the boundary layer. *Journal of the Atmospheric Sciences*, *32*(4), 753–766. https://doi.org/10.1175/1520-0469(1975)032<0753:TVTOKE>2.0.CO;2

McWilliams, J. C., Sullivan, P. P., & Moeng, C.-H. (1997). Langmuir turbulence in the ocean. *Journal of Fluid Mechanics*, *334*, 1–30. https://doi.org/10.1017/S0022112096004375

Melville, W. K. (1996). The role of surface-wave breaking in Air-Sea Interaction. *Annual Review of Fluid Mechanics*, *28*(1), 279–321. https://doi.org/10.1146/annurev.fl.28.010196.001431

Miles, J. W. (1957). On the generation of surface waves by shear flows. *Journal of Fluid Mechanics*, *3*(2), 185–204. https://doi.org/10.1017/S0022112057000567

Noh, Y., Ok, H., Lee, E., Toyoda, T., & Hirose, N. (2016). Parameterization of Langmuir circulation in the ocean mixed layer model using LES and its application to the OGCM. *Journal of Physical Oceanography*, *46*(1), 57–78. https://doi.org/10.1175/JPO-D-14-0137.1

Park, J., Lindberg, C. R., & Vernon, F. L., III. (1987). Multitaper spectral analysis of high-frequency seismograms. *Journal of Geophysical Research*, *92*(B12), 12675–12684. https://doi.org/10.1029/JB092iB12p12675

Phillips, O. M. (1957). On the generation of waves by turbulent wind. *Journal of Fluid Mechanics*, *2*(05), 417–445. https://doi.org/10.1017/s0022112057000233

Piper, M., & Lundquist, J. K. (2004). Surface layer turbulence measurements during a frontal passage. *Journal of the Atmospheric Sciences*, *61*(14), 1768–1780. https://doi.org/10.1175/1520-0469(2004)061<1768:SLTMDA>2.0.CO;2

Plant, W. J. (1982). A relationship between wind stress and wave slope. *Journal of Geophysical Research*, *87*(March), 1961–1967. https://doi.org/10.1029/JC087iC03p01961

21699291, 2024, 8, Downloaded from https://agupubs.onlinelibrary.wiley.com/doi/10.1029/2023JC020308 by Christopher J Zappa - Columbia University Libraries , Wiley Online Library on [16/08/2024]. See the Terms and Conditions (https://onlinelibrary.wiley.com/terms-and-conditions) on Wiley Online Library for rules of use; OA articles are governed by the applicable Creative Commons License

Reul, N., Branger, H., & Giovanangeli, J.-P. (1999). Air flow separation over unsteady breaking waves. *Physics of Fluids*, *11*(7), 1959–1961. https://doi.org/10.1063/1.870058

Schwendeman, M., Thomson, J., & Gemmrich, J. R. (2013). Wave breaking dissipation in a young wind sea. *Journal of Physical Oceanography*, *44*(1), 104–127. https://doi.org/10.1175/JPO-D-12-0237.1

Scully, M. E., Trowbridge, J. H., & Fisher, A. W. (2016). Observations of the transfer of energy and momentum to the oceanic surface boundary layer beneath breaking waves. *Journal of Physical Oceanography*, *46*(6), 1823–1837. https://doi.org/10.1175/JPO-D-15-0165.1

Semedo, A., Saetra, Ø., Rutgersson, A., Kahma, K. K., & Pettersson, H. (2009). Wave-induced wind in the marine boundary layer. *Journal of the Atmospheric Sciences*, *66*(8), 2256–2271. https://doi.org/10.1175/2009JAS3018.1

Sentchev, A., Forget, P., & Fraunié, P. (2017). Surface current dynamicsunder sea breeze conditions observed by simultaneous HF radar, ADCP and drifter measurements. *Ocean Dynamics*, *67*(February), 499–512. https://doi.org/10.1007/s10236-0171035-6

Shaikh, N., & Siddiqui, K. (2011). Near-surface flow structure over wind-generated water waves, Part I: Wave-induced flow characteristics. *Ocean Dynamics*, *61*(1), 127–141. https://doi.org/10.1007/s10236-010-0361-8

Sjöblom, A., & Smedman, A.-S. (2003). Vertical structure in the marine atmospheric boundary layer and its implication for the inertial dissipation method. *Boundary-Layer Meteorology*, *109*(1), 1–25. https://doi.org/10.1023/A:1025407109324

Snyder, R. L., Dobson, F. W., Elliott, J. A., & Long, R. B. (1981). Array measurements of atmospheric pressure fluctuations above surface gravity waves. *Journal of Fluid Mechanics*, *102*, 1–59. https://doi.org/10.1017/S0022112081002528

Soloviev, A., & Lukas, R. (2003). Observation of wave-enhanced turbulence in the near-surface layer of the ocean during TOGA COARE. *Deep Sea Research Part I: Oceanographic Research Papers*, *50*(3), 371–395. https://doi.org/10.1016/S0967-0637(03)00004-9

Sullivan, P. P., McWilliams, J. C., & Kendall Melville, W. (2007). Surface gravity wave effects in the oceanic boundary layer: Large-eddy simulation with vortex force and stochastic breakers. *Journal of Fluid Mechanics*, *593*, 405–452. https://doi.org/10.1017/S002211200700897X

Sutherland, G., Ward, B., & Christensen, K. H. (2013). Wave-turbulence scaling in the ocean mixed layer. *Ocean Science*, *9*(4), 597–608. https://doi.org/10.5194/os-9-597-2013

Sutherland, P., & Kendall Melville, W. (2015). Field measurements of surface and near-surface turbulence in the presence of breaking waves. *Journal of Physical Oceanography*, *45*(4), 943–965. https://doi.org/10.1175/JPO-D-14-0133.1

Tennekes, H., & Lumley, J. L. (1972). A first course in turbulence. Retrieved from https://api.semanticscholar.org/CorpusID:116935579

Terray, E. A., Donelan, M. A., Agrawal, Y. C., Drennan, W. M., Kahma, K. K., Williams, A. J., et al. (1996). Estimates of kinetic energy dissipation under breaking waves. *Journal of Physical Oceanography*, *26*(5), 792–807. https://doi.org/10.1175/1520-0485(1996)026<0792:EOKEDU>2.0.CO;2

The MathWorks Inc. (2022). *MATLAB version: 9.13.0 (R2022b)*, The MathWorks Inc. Retrieved from https://www.mathworks.com

Thomson, J. (2012). Wave breaking dissipation observed with 'SWIFT' drifters. *Journal of Atmospheric and Oceanic Technology*, *29*(12), 1866–1882. https://doi.org/10.1175/JTECH-D-12-00018.1

Thomson, J., Schwendeman, M. S., Zippel, S. F., Moghimi, S., Gemmrich, J., & Erick Rogers, W. (2016). Wave-breaking turbulence in the ocean surface layer. *Journal of Physical Oceanography*, *46*(6), 1857–1870. https://doi.org/10.1175/JPO-D-15-0130.1

Toba, Y., & Kawamura, H. (1996). Wind-wave coupled Downward-Bursting Boundary Layer (DBBL) beneath the sea surface. *Journal of Oceanography*, *52*(4), 409–419. https://doi.org/10.1007/BF02239046

Wetzel, S. W. (1996). An investigation of wave-induced momentum flux through phase averaging of open ocean wind and wave fields. Retrieved from https://api.semanticscholar.org/CorpusID:14931719

Wiles, P. J., Rippeth, T. P., Simpson, J. H., & Hendricks, P. J. (2006). A novel technique for measuring the rate of turbulent dissipation in the marine environment. *Geophysical Research Letters*, *33*(21), L21608. https://doi.org/10.1029/2006GL027050

Wu, L., Breivik, Ø., & Rutgersson, A. (2019). Ocean-Wave-Atmosphere interaction processes in a fully coupled modeling system. *Journal of Advances in Modeling Earth Systems*, *11*(11), 3852–3874. https://doi.org/10.1029/2019MS001761

Wyngaard, J. C., & Clifford, S. F. (1977). Taylor's hypothesis and high–frequency turbulence spectra. *Journal of the Atmospheric Sciences*, *34*(6), 922–929. https://doi.org/10.1175/1520-0469(1977)034<0922:thahts>2.0.co;2

Wyngaard, J. C., & Coté, O. R. (1971). The budgets of turbulent kinetic energy and temperature variance in the atmospheric surface layer. *Journal of the Atmospheric Sciences*, *28*(2), 190–201. https://doi.org/10.1175/1520-0469(1971)028<0190:TBOTKE>2.0.CO;2

Zhang, H., & Talley, L. D., (1998). Heat and buoyancy budgets and mixing rates in the upper thermocline of the Indian and global oceans. *Journal of Physical Oceanography*, *28*(10), 1961–1978. https://doi.org/10.1175/1520-0485(1998)028<1961:HABBAM>2.0.CO;2

Zippel, S. F., Edson, J. B., Scully, M. E., & Keefe, O. R. (2024). Direct observation of wave-coherent pressure work in the atmospheric boundary layer. *Journal of Physical Oceanography*, *54*(2), 445–459. https://doi.org/10.1175/JPO-D-23-0097.1

Zippel, S. F., Thomas Farrar, J., Zappa, C. J., & Plueddemann, A. J. (2022). Parsing the kinetic energy budget of the ocean surface mixed layer. *Geophysical Research Letters*, *49*(2), e2021GL095920. https://doi.org/10.1029/2021GL095920

21699291, 2024, 8, Downloaded from https://agupubs.onlinelibrary.wiley.com/doi/10.1029/2023JC020308 by Christopher J Zappa - Columbia University Libraries , Wiley Online Library on [16/08/2024]. See the Terms and Conditions (https://onlinelibrary.wiley.com/terms-and-conditions) on Wiley Online Library for rules of use; OA articles are governed by the applicable Creative Commons License